Numerical study on the aerodynamics of an iced airfoil with scale-resolving simulations

Man Long Wong*, Aditya S. Ghate†, Gerrit-Daniel Stich‡, Gaetan K. Kenway§, and Cetin C. Kiris¶
NASA Ames Research Center, Moffett Field, CA 94035

Scale-resolving simulations of the NACA 23012 airfoil with horn ice accretion on the leading edge are conducted using the hybrid Reynolds-averaged Navier–Stokes/large-eddy simulation (hybrid RANS/LES) and wall-modeled large-eddy simulation (WMLES) approaches implemented in the Launch, Ascent, and Vehicle Aerodynamics (LAVA) framework. Aerodynamic results at the Reynolds number of 1.8 million show good comparison with the experimental measurements at different angles of attack from pre-stall to post-stall regimes. The pressure plateaus caused by the flow separation and the recovery of pressure inside the separation bubble around the iced leading edge are well predicted with the scale-resolving simulations when sufficient grid resolution is used around the accreted ice. The unsteadiness of the turbulent flows around the iced airfoil is also examined through the turbulent kinetic energy with the Reynolds normal stress anisotropy. Kelvin–Helmholtz instability (KHI) arises at the shear layer triggered by the upper ice horn and leads to rapid laminar-to-turbulent transition over a large range of angle of attack. With the increase of the angle of attack, the region with high turbulence intensity induced by the unstable shear layer spreads quickly over the entire upper surface of the airfoil. The coherent KHI modes from the upper and lower ice horns are extracted using the spectral proper orthogonal decomposition (SPOD) technique. The SPOD modes extracted from the upper shear layer have large-scale variations in the spanwise direction and low-rank behavior where the energy of the leading SPOD mode at each Strouhal number of the KHI largely represents the total energy when the mode number in the spanwise direction is small.

I. Introduction

The performance of an aircraft can be largely degraded when the aerodynamic devices are contaminated with ice. The ice accretion on the lifting surfaces can cause major reduction in the maximum lift coefficient and the stall angle of attack, and thus can pose threat to flight safely. In addition, the drag is increased and this leads to more fuel consumption and decreased maximum flight range. As a result, the study of ice accretion and its influence on aerodynamics is critical for aircraft design and certification. In general, the ice shapes can be summarized into the categories of roughness ice, horn ice, streamwise ice, and spanwise-ridge ice [1]. These ice shapes are formed at different stages of the ice accretion process under different flight conditions. The actual ice geometry may also have features composed of two or more of these ice shape types. These various ice shapes have different aerodynamic effects and hence complicate the study of iced aerodynamics.

Since the NASA's aircraft icing program in 1978 [2], there have been numerous experimental studies on the effects of ice shapes on modern airfoils and wings [3–8]. In these studies, different ice shape configurations were first determined from iced tunnels and then castings of these ice shapes were fabricated and placed on models for aerodynamic measurements in dry wind tunnels. The effects of Reynolds and Mach numbers [3, 4, 6, 9], as well as the comparison between two-dimensional (2D) and three-dimensional (3D) ice accretions [9, 10] were examined in these experimental works. While these experimental studies improve the understanding of iced aerodynamics, they are extremely expensive to perform. In order to fully simulate the aerodynamics of any aerodynamic devices with ice accretion using numerical calculations, modeling the formation of ice shapes given the flight conditions and the accurate predictions of the overall turbulent flow fields around the iced geometries are both critical. One of the main objectives of this work focuses on the examination of affordable and accurate computational approaches to meet the latter requirement. Various

*Science and Technology Corporation, AIAA Member, manlong.wong@nasa.gov.
†Science and Technology Corporation, AIAA Member, aditya.s.ghate@nasa.gov.
‡Science and Technology Corporation, AIAA Member, gerrit-daniel.stich@nasa.gov.
§Science and Technology Corporation, AIAA Member, gaetan.k.kenway@nasa.gov.
¶Computational Aerosciences Branch, AIAA Senior Member, cetin.c.kiris@nasa.gov.

modeling approaches were attempted in previous literature. An early computational approach employed for studying iced aerodynamics is the Reynolds-averaged Navier–Stokes (RANS) method where additional turbulent modeling terms or equations are added to the Navier–Stokes equations for steady or quasi-steady solutions using steady RANS and unsteady RANS simulations respectively. While this approach is very cost effective, it tends to over-predict the upper surface pressure and under-predict the lift coefficient and the stall angle [11–13]. The scale-resolving simulation or large-eddy simulation (LES) is a more promising approach where energy-containing scales are well-resolved while the effects from small turbulent eddies are modeled by subgrid-scale (SGS) models. For external aerodynamics problems, wall treatments are also of paramount importance for LES computations to eliminate the tremendous computational cost in resolving the thin boundary layers. The hybrid Reynolds-averaged Navier–Stokes/large-eddy simulation (RANS/LES) and the wall-modeled LES (WMLES) are two popular scale-resolving simulation approaches with wall treatments for external aerodynamics. Belonging to the hybrid RANS/LES approach, the detached-eddy simulation (DES) [14, 15], delayed detached eddy simulation (DDES) [16], zonal DES (ZDES) [17], and dynamic hybrid RANS/LES method (DHRL) [18], were used for studying iced airfoils or wings. In the hybrid RANS/LES approach, RANS model is used for the inner layer of the boundary layer and LES only exists for the outer layer or the flow separated regions. Compared with the RANS calculations, simulations performed with the hybrid RANS/LES approach generally showed better predictions on the lift and drag coefficients, and the flow features around the ice-accreted airfoils or wings, such as the separation bubbles. However, ineffectiveness in predicting the Kelvin–Helmholtz instability (KHI) was also reported for some hybrid RANS/LES computations [17]. Recently, there have been some studies on the use of WMLES for iced aerodynamics study [19, 20]. In contrast to the hybrid RANS/LES approach, LES solutions are computed all the way to the walls and the velocity and temperature gradients at the rigid solid boundaries are obtained with modeled shear stress and heat flux boundary conditions [21]. It was reported that the WMLES approach is capable of accurately predicting the flow separation around iced airfoils and the KHI of the free shear layers [19].

In this work, hybrid RANS/LES using an improved version of ZDES and WMLES with an algebraic wall model are conducted for the NACA 23012 with artificial horn ice accretion using the Launch, Ascent, and Vehicle Aerodynamics (LAVA) framework [22]. Both the hybrid RANS/LES and WMLES approaches are coupled with a penalty immersed boundary method using source terms [23]. In this strategy, body-fitted curvilinear overset meshes are built for the clean airfoil while the effects of ice accretion at the leading edge are imposed with the penalty immersed boundary method. The numerical results from the hybrid RANS/LES and WMLES approaches coupled with the penalty immersed boundary method are presented and compared with the experimental results. With the scale-resolving simulation results, the fluctuations of the turbulent flows around the airfoil are studied through different statistical quantities. Modal analysis of the KHI at the shear layers induced by the ice is also performed using the spectral proper orthogonal decomposition technique with time-resolved data.

This paper is organized as follows. In Section II, the iced airfoil benchmark problem is first introduced in details. Then, the hybrid RANS/LES and WMLES turbulence approaches, as well as the penalty immersed boundary method and the numerical methods, are presented in Section III. In Section IV, the details on the overset curvilinear meshes and the simulation strategies used are provided. The visualizations of the flows around the iced airfoil from different simulations are shown in Section V, which is followed by the comparison of the aerodynamic quantities including the lift, drag, pitching moment, and surface pressure from the numerical calculations with the experimental measurements in Section VI. In Section VII, the turbulent kinetic energy with the Reynolds stress anisotropy and the coherent modes of the KHI at the shear layers extracted using the spectral proper orthogonal method are studied for better understanding of the flow physics of the chosen iced airfoil problem. Finally, Section VIII summarizes our findings in this work.

II. Problem Description

A flow past an airfoil with an artificial horn ice accreted at the leading edge is simulated in this work using scaling-resolving simulations. This configuration, EG1164, is adopted from one of the six iced NACA 23012 airfoil cases in [6]. The aerodynamic data of this case, together with another five cases, at the chord-based Reynolds number, $Re = 1.8 \times 10^6$, and the free-stream Mach number, $M = 0.18$, was measured at the dry wind tunnel of the University of Illinois using a 18-inch NACA 23012 airfoil model (chord length $c = 0.4572$ m) with different ice-shape castings. The artificial iced airfoil models have geometrically down-scaled shapes created with constant cross section extrusion of the 2D tracings of the spanwise-averaged 3D full-scale ice accretion geometries. The 3D full-scale ice shapes were generated in the NASA Glenn's Icing Research Tunnel (IRT). Iced airfoils with full-scale 3D castings were also tested in the ONERA F1 wind tunnel at higher Reynolds and Mach numbers, $Re = 15.9 \times 10^6$ and $M = 0.2$ [6]. In a previous work [24], the subscale iced airfoil wind tunnel results were compared with the full-scale results. The aerodynamic

coefficients of the subscale Reynolds number EG1164 case with the 2D smooth model were found to be similar to the case with full-scale casting at the higher Reynolds number. The difference in maximum lift coefficient, $C_{l,max}$, of the subscale and full-scale cases is within 2%. As a result, the subscale EG1164 case is adopted in this work as this 2D iced airfoil case can be simulated with periodic spanwise direction (y-direction). The 2D tracing of the cross section of the EG1164 case near the leading edge on the x-z plane is depicted in Figure 1(a). The upper horn has a height of around $0.020c$ and is located at $x \approx 0.009c$. The angle of the horn with respect to the airfoil chord line is around 27°. We have chosen a spanwise length of $0.5c$ and the 3D computational model of the iced-airfoil is shown in Figure 1(b).

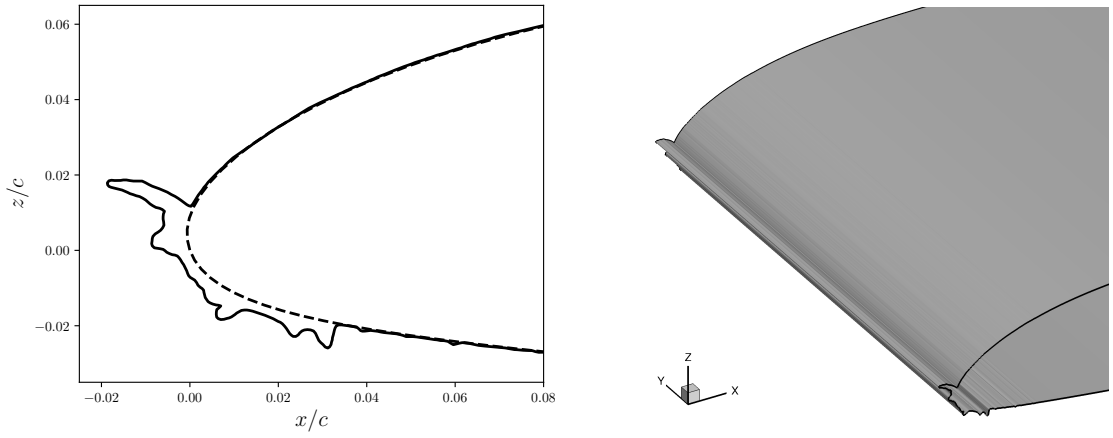

2D airfoil tracings [6, 9]
(a) Solid line: EG1164; dashed line: NACA 23012

(b) 3D model

Fig. 1 Shape of the EG1164 iced airfoil near the leading edge.

III. Turbulence Models and Numerical Methods

Both the hybrid RANS/LES and WMLES approaches are adopted as the scale-resolving simulation methods for comparison in this work. Figure 2 shows certain algorithmic and philosophical differences between hybrid RANS/LES and WMLES. In the hybrid RANS/LES method, the attached boundary layer and the separated flow should be simulated in RANS and LES modes respectively. The switch between the RANS and LES modes is usually determined by comparing the wall distance and the local grid resolution. On the other hand, the WMLES is based on a global LES closure of the flow field and the wall stress and heat flux boundary conditions are given by the wall model using LES solutions close to but not on the wall. This leads to different requirements on the grids, where the unit normalized wall distance of the first cell node, $\Delta y^+ = 1$, is required for the hybrid RANS/LES approach to obtain well-resolved boundary layer solutions in the RANS mode while highly isotropic grid up to the wall is generally used for WMLES calculations in practice.

A. Hybrid RANS/LES

The ZDES mode 2 with enhanced protection (EP) [26] is employed in this work for the hybrid RANS/LES computations. The ZDES mode 2 with EP has two improvements over the previous hybrid RANS/LES methods such as the DDES [27] and the original ZDES mode 2 [28]. Firstly, the shielding is improved with a second shielding function to ensure that the RANS mode instead of the LES mode is used in the attached boundary layers. Secondly, the delay issue in regards to the formation of instabilities is alleviated by the introduction of an inhibition function to switch off the second shielding function and the enhancement of the destruction of eddy viscosity in the gray areas where the solution is neither pure RANS nor pure LES. When the solution is in RANS mode, the Spalart–Allmaras (SA) turbulence model [29] is used to close the Reynolds-averaged Navier–Stokes equation with Favre averaging on the conservative equations. The maximum edge length for a grid cell serves as the local length scale used in the LES SGS closure. The ZDES mode 2 with EP implemented in LAVA has been validated in multiple previous works such as [30–33].

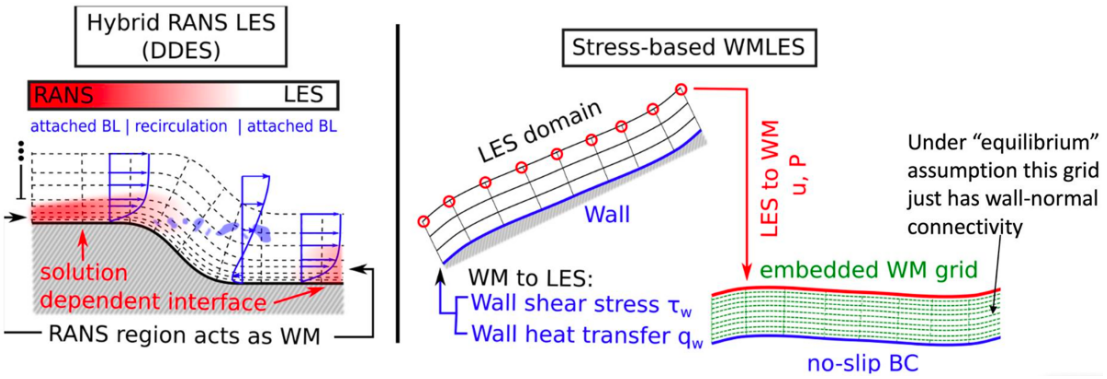

Fig. 2 Schematic depicting the fundamental algorithmic differences between hybrid RANS/LES (left) and WMLES (right) [25].

B. WMLES

In the wall-stress WMLES approach, the LES solutions are computed all the way to the walls with wall stress and heat flux boundary conditions provided by the wall models (WMs), whereas the wall models use the LES solutions close to the wall as outer boundary conditions. The WMLES method considered in this work is a physics-based approach which can be simply categorized into the algebraic, ordinary differential equation (ODE) based, and partial differential equation (PDE) based models. The most general method is the PDE-based one where the thin boundary layer (TBL) PDE are solved with most or all of the terms in the left hand side of the equations retained. However, a near wall separate RANS grid is required in this method for solving the TBL PDE, apart from the LES grid. A computationally more affordable method is the ODE-based equilibrium WMLES where the exact balance of the left hand side terms in the TBL PDE are assumed, thus only ODE are solved. In this work, the less expensive algebraic equilibrium WMLES is used where approximate solutions to the ODE-based equilibrium WMLES are sought through algebraic equations with a nonlinear solver. More details on the wall-stress WMLES can be found in the previous literature review articles [21, 34–36]. The algebraic wall model implemented in this work is an analytical law with smooth blending between the viscous sublayer and log-layer. All WMLES runs use the Vreman SGS model [37] with a fixed model constant set as $c_{\text{sgs}} = 0.08$. The WMLES in LAVA has been used successfully for a variety of applications [32, 38–42].

C. Numerical Discretizations

The convective flux derivatives are approximated using second order finite differencing of numerical fluxes at midpoints. The numerical fluxes are computed with the left- and right-biased interpolated primitive variable vectors using an approximate Riemann solver, where the modified Roe Riemann solver is used in this work. The interpolation is a fourth order central interpolation nonlinearly blended with the third order left or right upwind-biased interpolations. Evaluation of the inviscid fluxes at midpoints, as opposed to nodes, results in reduced aliasing errors and hence improves nonlinear robustness for turbulent flows. In general, the blended interpolations are essentially reduced to the central interpolation in turbulent regions. The concept of nonlinear blending between upwind-biased and central interpolations is similar to [43] but the sensor used in this work is a physics-based sensor that compares the magnitudes between the vorticity and the dilatation to detect turbulent regions. The interpolations are forced to be upwind-biased at overset fringe points to enhance robustness and reduce numerical artifacts which may occur near overset boundaries. The viscous and diffusive flux vectors are evaluated at the midpoints using second order accurate staggered finite differencing, followed by a second order accurate scheme for the derivatives. For the time integration in the hybrid RANS/LES runs, the implicit second order backward difference formulation (BDF2) is used in physical time, along with pseudo-time embedding and incomplete LU factorization (ILU(1)) preconditioned generalized minimal residual (GMRES) method. As for the WMLES runs, the explicit third order total variation diminishing Runge–Kutta (RK-TVD) [44] time stepping scheme is employed.

D. Penalty Immersed Boundary Method

In the problem considered, the ice accreted on the airfoil surface has a complex shape and tiny characteristic length scales that pose a challenge for body-fitted mesh generation. Nevertheless, the ice is only accreted on a limited region of the airfoil surface near the leading edge. Most of the airfoil surface is clean and not covered by any ice. The clean airfoil surface geometry is smooth where a body-fitted mesh can be made around it without much human effort. In this work, the hybrid body-fitted (BF)/immersed boundary (IB) approach similar to a previous work [23] is adopted for both the hybrid RANS/LES and WMLES calculations. In the hybrid BF/IB approach, a body-fitted structured mesh is used for the smooth and clean geometry while IB method is applied locally with spatio-temporal source or penalty terms near the complex geometric features adhered on the smooth surface. This is different than the global IB approach where the walls are modeled with IB conditions only. Due to the grid requirement (unit normalized wall distance at the first cell node) for hybrid RANS/LES, the use of the global IB approach requires high mesh resolution near the walls. In addition, the hybrid BF/IB approach is a robust, incremental, and easy to implement method for any mature body-fitted code such as the curvilinear LAVA code where the hybrid RANS/LES and WMLES capabilities [30–33, 33, 38–40] were well validated for many aerodynamics applications. The hybrid BF/IB approach has been shown to work well for different applications such as afterbody flow with a serrated skirt [45] and full space launcher [23]. In this work, no-slip boundary conditions are enforced at the horn ice using the penalty method while hybrid RANS/LES or WMLES boundary treatments are used for the remaining part of the airfoil that is not covered by ice. The capabilities of these hybrid BF/IB approaches for the chosen iced airfoil case are examined in this work to provide a preliminary investigation on the approaches for more complicated iced aerodynamics applications such as iced swept wings [46, 47].

IV. Overset Curvilinear Meshes and Simulation Strategies

Overset curvilinear meshes are used for the hybrid RANS/LES and WMLES calculations. A baseline mesh and an improved mesh are designed for the WMLES runs. Both the baseline and improved meshes are highly isotropic in regions close to the airfoil up to the walls. The overset WMLES meshes near the leading edge of the airfoil are shown in Figure 3. Both meshes are generated around the airfoil assuming there is no ice accretion on the airfoil leading edge. In the simulations with the hybrid BF/IB approach, surface mesh that defines the shape of the ice is supplied and grid cells beneath the surface mesh are tagged as solid cells. Using the penalty method, the boundary conditions are imposed on the ice surface and the flow inside the solid cells is driven to zero using source terms. The baseline and improved WMLES meshes are similar except that the latter has refined grids near the horn ice and the leading edge which are colored in magenta in the figure. The hybrid RANS/LES mesh has resolution similar to that of the improved WMLES far away from the wall. However, the mesh of the former is much finer near wall than that of the latter to satisfy the constraint of unit normalized wall distance at first cell node. As a result, the near-wall cells of the hybrid RANS/LES mesh are highly anisotropic, as shown in Figure 4. The details of the grid spacings, numbers of grid cells, and the time step sizes are presented in Table 1. The time step sizes for the WMLES cases are the approximated values with an acoustic Courant–Friedrichs–Lewy (CFL) number of 1.5, which is found to be sufficiently robust with the explicit time stepping method. Note that even with very small grid spacing near the walls, the time step size of the hybrid RANS/LES calculations can be one order of magnitude larger than those of the WMLES runs, because of the robustness given by the implicit time stepping (BDF2) used in the former. As suggested in [33], the time step size of the hybrid RANS/LES has to be large to save computational cost but also needs to be small enough to resolve the turbulent features for accurate aerodynamics predictions. As a result, the time step size of the hybrid RANS/LES runs is chosen to be close to that given by the unit incompressible CFL number based on the compromise. The penalty IB method requires the user's specification of a time scale for the penalty source terms. A smaller time scale imposes more accurate boundary effects as the penalty source terms act at a faster rate. However, numerical difficulties are encountered with the explicit time stepping method when the time scale for the IB method is smaller than the time step size given by the acoustic CFL conditions. Therefore, the time scale for the IB method is chosen to be slightly larger than the explicit time step size for the WMLES runs. On the other hand, as the implicit time stepping is used for the hybrid RANS/LES runs, a penalty time scale that is one order of magnitude smaller than the WMLES runs can be chosen robustly. The penalty IB time scales of different cases are given in Table 1.

Four angles of attack at $\alpha = 6.2°$, $\alpha = 8.0°$, $\alpha = 9.0°$, and $\alpha = 10.0°$ are chosen for the hybrid RANS/LES and WMLES calculations, where $\alpha = 10.0°$ is a post-stall angle of attack. The WMLES runs with the baseline mesh are initialized from the free-stream conditions (cold start) and those with the improved mesh are initialized using the baseline mesh solutions interpolated to the finer grids. The simulations of hybrid RANS/LES are initialized with the steady RANS solutions using the SA turbulence model. 50 convective time units (CTUs) are used to flush out the initial

transients for all simulations where the CTU is based on the chord length and the free-stream velocity magnitude. The data sampling continues for 50 CTUs at $\alpha = 6.2°$ and $\alpha = 8.0°$ and 100 CTUs at $\alpha = 9.0°$ and $\alpha = 10.0°$. It is found that large numbers of CTUs are required to get time-converged mean aerodynamic statistics for the higher angles of attack because of the low frequency fluctuations in the aerodynamic loads and moments. Unsteady RANS simulations using the SA turbulence model are also conducted to provide the aerodynamic loads and pitching moments at the four angles of attack for the scale-resolving simulations to be compared with. A 2D mesh which is basically a x-z cut-plane of the hybrid RANS/LES mesh is used for the unsteady RANS runs. The numerical methods and simulation strategies used for the unsteady RANS are similar to the hybrid RANS/LES but the upwind-biased interpolation, instead of the blended central/upwind-biased interpolation, is used in the entire computational domain for computing the convective flux and a larger time step size of 1% CTU is used with the BDF2 time stepping.

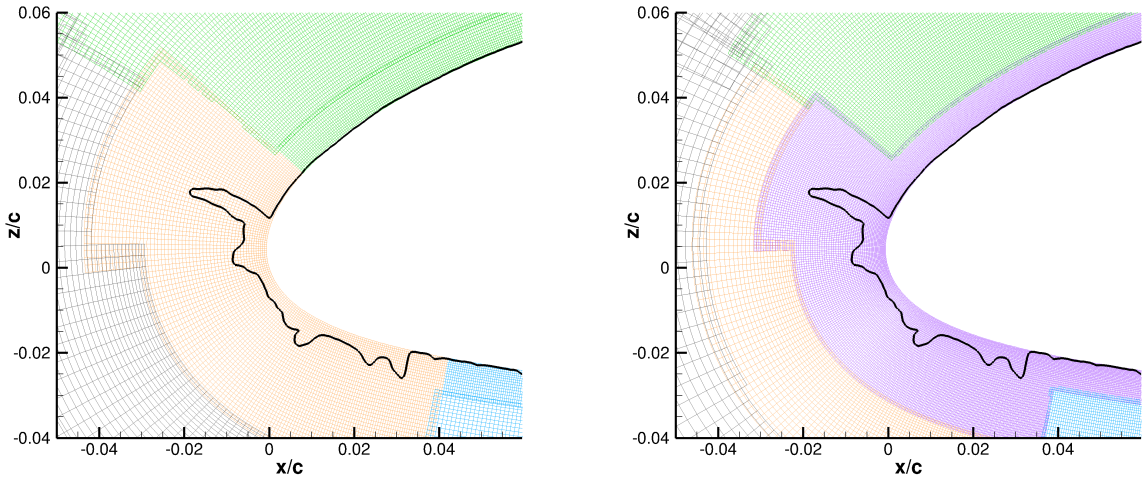

(a) Baseline WMLES mesh

(b) Improved WMLES mesh

Fig. 3 The baseline and improved overset curvilinear meshes for the WMLES runs near the iced leading edge. The improved mesh has grids colored in magenta with improved grid resolution around the horn ice and the leading edge compared to the base mesh. The black thick contour line represents the location of the surface mesh that defines the shape of the ice accreted on the airfoil where grid cells inside it are treated as solid cells.

Grid	Minimum wall normal grid spacing ($\times 10^{-3}$ c)	Minimum grid spacing in other directions ($\times 10^{-3}$ c)	Number of grid cells (million)	Time step size ($\times 10^{-5}$ CTU)	Time scale of IB ($\times 10^{-5}$ CTU)
hybrid RANS/LES	0.014	0.243	367.7	24.94	0.14
WMLES-baseline	0.486	0.486	119.1	~ 3.82	4.09
WMLES-improved	0.243	0.243	206.6	~ 1.91	2.04

Table 1 The details of different grids used for hybrid RANS/LES and WMLES. Unit normalized wall distance at first cell node is targeted for hybrid RANS/LES.

V. Flow Visualizations

The instantaneous iso-surfaces of Q-criterion from the simulations using the hybrid RANS/LES and the WMLES with the improved mesh, normalized by the free-stream velocity magnitude, U_∞, and chord length, c, at different angles of attack are displayed in Figure 5. The iso-surfaces are colored by the streamwise velocity component, u, normalized by U_∞. From these iso-surfaces, flow separation can be seen behind the upper horn near the leading edge for each angle of attack. The separated flows form free shear layers and separation bubbles downstream of the horn. Due to the KHI caused by the large velocity difference across the shear layers, there is roll-up of spanwise vortices at the shear

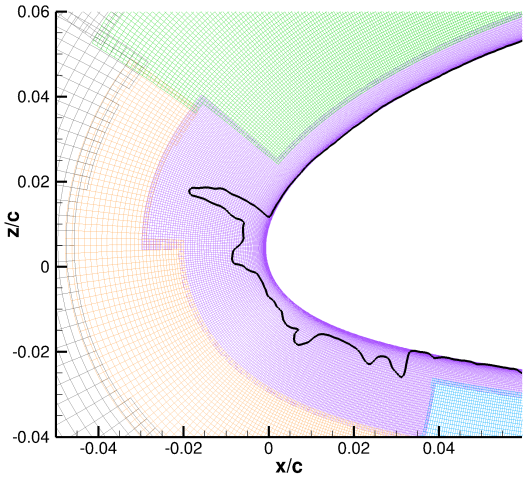

Fig. 4 The overset curvilinear mesh for the hybrid RANS/LES runs near the iced leading edge. The grids colored in magenta have normalized wall distance of one at the first cell node and similar grid resolution as the improved mesh for the WMLES runs far away from the wall. The black thick contour line represents the shape of the ice accretion similar to Figure 3.

layers. Initially, there are only large-scale variations in the spanwise direction for these vortices. As these vortices advect downstream, they cannot maintain themselves and finally break down into 3D turbulent eddies. The shear mixing layers are energized during the laminar-to-turbulent transitions and reattach to the upper surface of the airfoil. After the reattachment, the boundary layers remain highly turbulent on the upper surface of the airfoil for all angles of attack. The iso-surfaces of the normalized instantaneous Q-criterion are very similar between the hybrid RANS/LES and the WMLES runs, especially in regions near the shear layers. While it was reported in earlier studies [17, 18] that the DES-type method can have difficulty in the prediction of KHI at the shear layer, this issue is not obvious in our hybrid RANS/LES runs. The ZDES mode 2 with EP is designed to alleviate the delay issue in the instability formation for the original ZDES mode 2. Using this improved ZDES mode 2, the vortex roll-up processes due to the KHI at the shear layers from our hybrid RANS/LES runs seem to be comparable with those from the WMLES runs at different angles of attack.

In Figure 6, the contours of the normalized instantaneous streamwise velocity component, u/U_∞, around the iced leading edge from different simulations on a x-z plane at $\alpha = 8^\circ$ are compared. From these contour plots, flow separation can be seen at various corners formed by the ice accretion on the upper and lower surfaces of the airfoil. Undoubtedly, the penalty immersed IB method successfully imposes the effects of the sharp corners to trigger the flow separation at these locations. Comparing the WMLES results with different grid resolutions around the horn ice, there are finer vortical features along the shear layer for the case with improved grid and this is not surprising as the improved grid has smaller grid cut-off to support finer flow features. The instantaneous velocity field from the hybrid RANS/LES run looks similar to the WMLES run with the improved mesh because of the same IB approach used at the horn ice and similar mesh resolution in regions around the shear layer.

The contours of normalized mean streamwise velocity component, $\overline{u}/U_\infty$, from the simulations of hybrid RANS/LES and WMLES with the improved mesh on a x-z plane are shown in Figure 7. The overline, $\overline{(\cdot)}$, denotes averaging in time. The magenta line on the upper airfoil surface near the leading edge in each plot indicates the location with zero streamwise velocity component and hence gives an estimation of the flow separation location, as well as the reattachment location of the shear layer and the size of the separation bubble. At the same angle of attack, the hybrid RANS/LES and WMLES results are similar but note that the hybrid RANS/LES predicts longer separation bubbles at $\alpha = 8.0^\circ$, $\alpha = 9.0^\circ$, and $\alpha = 10.0^\circ$, compared to WMLES. From these plots, it can be seen that as the angle of attack increases, the size of the separation bubble at the leading edge increases. For the post-stall angle of attack, $\alpha = 10^\circ$, both hybrid RANS/LES and WMLES results show another flow separation similarly on the upper surface starting from $x \approx 0.6c$, indicating stall. At $\alpha = 6.2^\circ$, $\alpha = 8.0^\circ$, $\alpha = 9.0^\circ$, and $\alpha = 10.0^\circ$, the reattachment locations of the leading edge

separation bubbles on the upper airfoil surface are $x = 0.061c$, $x = 0.102c$, $x = 0.210c$, and $x = 0.218c$ respectively for the hybrid RANS/LES runs and $x = 0.058c$, $x = 0.086c$, $x = 0.157c$, and $x = 0.159c$ respectively for the WMLES runs. It is suggested in [19, 48] that the reattachment point on the upper surface scales as the square of the angle of attack for the NLF 0414 iced airfoil with horn features. However, we have found that performing least-square fittings with $(x/c)_{reattach} = a\alpha^2 + b$ for the constants a and b with our simulated reattachment locations, $(x/c)_{reattach}$ at the lower three angles of attack can give up to 26% and 20% errors respectively for the hybrid RANS/LES and WMLES computations of the EG1164 iced airfoil.

VI. Aerodynamic Loads, Pitching Moments, and Pressure Coefficients

The coefficients of lift (C_l), drag (C_d), and pitching moment (C_m) against the angle of attack from different scale-resolving simulations and the unsteady RANS runs are compared with the experimental results in Figure 8. These aerodynamic coefficients are computed with averaging in time and spanwise direction. As discussed in the earlier section, there are two sets of experimental data respectively at the subscale and full-scale Reynolds numbers for the EG1164 case. The numerical results should be compared with the results of the subscale Reynolds number case where a simplified and geometrically down-scaled iced airfoil model with constant cross-section extrusion was used in the wind tunnel tests. The full-scale Reynolds number data was collected using an iced airfoil with full-scale 3D ice accretion casting and is included in the plots as a reference. The two experimental results have similar maximum lift coefficients of $C_{l,max} \approx 0.86$ [24]. The lack of significant Reynolds number effects, particularly on the lift, is generally true for iced airfoils, in contrast to the large Reynolds number effects on clean airfoils in the Reynolds number range of interest. From the figure, it can be seen that the $C_{l,max}$ of the clean NACA23012 airfoil is around 1.4 at the subscale Reynolds number and the stall angle of attack is $\alpha = 14.4^\circ$ [49]. The ice accretion on the airfoil has large detrimental effects on the aerodynamics as the maximum lift coefficient drops by roughly 39% and the stall angle is reduced by around 5.6°. The lift coefficients obtained from the hybrid RANS/LES and the WMLES with the improved mesh are quite similar to each other and compare very well with the experimental values at different angles of attack except at $\alpha = 10.0^\circ$. On the other hand, the lift coefficient predicted with the unsteady RANS is only accurate at 6.2°. As the angle of attack increases, there is larger under-prediction in lift for the unsteady RANS. In fact, the unsteady RANS results even suggest the iced airfoil to stall at an angle of attack between 8.0° and 9.0°, which is definitely too early compared to the experimental results. Grid sensitivity on C_l at $\alpha = 9.0^\circ$ can be seen between the WMLES results computed with the baseline and improved meshes and the latter agrees better with the experimental C_l and this is possibly improved by more accurate representation of the horn ice with finer grid resolution. At $\alpha = 10.0^\circ$, the mean lift coefficients from different numerical runs are close to each other but are under-predicted compared with the experimental value. In fact, the fluctuations in C_l from the numerical simulations are large at this post-stall angle of attack. The time histories of the lift coefficients from the simulations of the hybrid RANS/LES and the WMLES with the improved mesh at different angles of attack are shown in Figure 9. From the plots, large fluctuations in time, t, at low frequencies can be seen for both the hybrid RANS/LES and WMLES calculations at $\alpha = 10.0^\circ$. The large fluctuations are measured using root mean squares (RMSs) which are shown as error bars in the lift coefficient plot. From Figure 9, smaller fluctuations in time at low frequencies can also be seen at $\alpha = 9.0^\circ$ and the hybrid RANS/LES run experiences larger fluctuation compared with the WMLES run. This is also reflected by the larger RMS of C_l from the hybrid RANS/LES run compared with the WMLES results at this angle of attack. With the ice accretion on the NACA23012 airfoil, both C_d and C_m are also significantly affected because of the large separation bubble near the leading edge. The drag coefficient of the iced airfoil is at least several times larger than that of the clean one, while the slope of the pitching moment coefficient is more positive from small angles of attack until the stall angle for the iced airfoil. All the scale-resolving simulations have very similar C_d and C_m values but with mild over-predictions at the lower angles of attack, $\alpha = 6.2^\circ$ and $\alpha = 8.0^\circ$. At higher angles of attack, the RMSs of these coefficients from the simulations become larger, similar to C_l. The WMLES predicts both C_d and C_m better than the hybrid RANS/LES at $\alpha = 9.0^\circ$ and the former also has smaller RMSs in these coefficients. The stall behavior is predicted reasonably well using either hybrid RANS/LES or WMLES as the pitching moment coefficients have successfully changed sign at $\alpha = 10.0^\circ$. Interestingly, the C_m from the scale-resolving simulations agree better with the full-scale experimental results rather than the subscale one at this post-stall angle of attack. Finally, the C_d and C_m results from the unsteady RANS seem to have reasonable agreements with the experimental values at different angles of attack. However, given the bad prediction capabilities on the lift, this fairly good comparison with the experimental results may be caused by error cancellations in the unsteady RANS.

The pressure coefficients, $C_p = 2(\overline{p} - p_\infty)/(\rho_\infty U_\infty^2)$, distributed on the surface of the iced airfoil at the angles of attack $\alpha = 6.2^\circ$ and $\alpha = 8.0^\circ$ are shown in Figure 10, where p, p_∞, and ρ_∞ are the surface pressure, free-stream pressure,

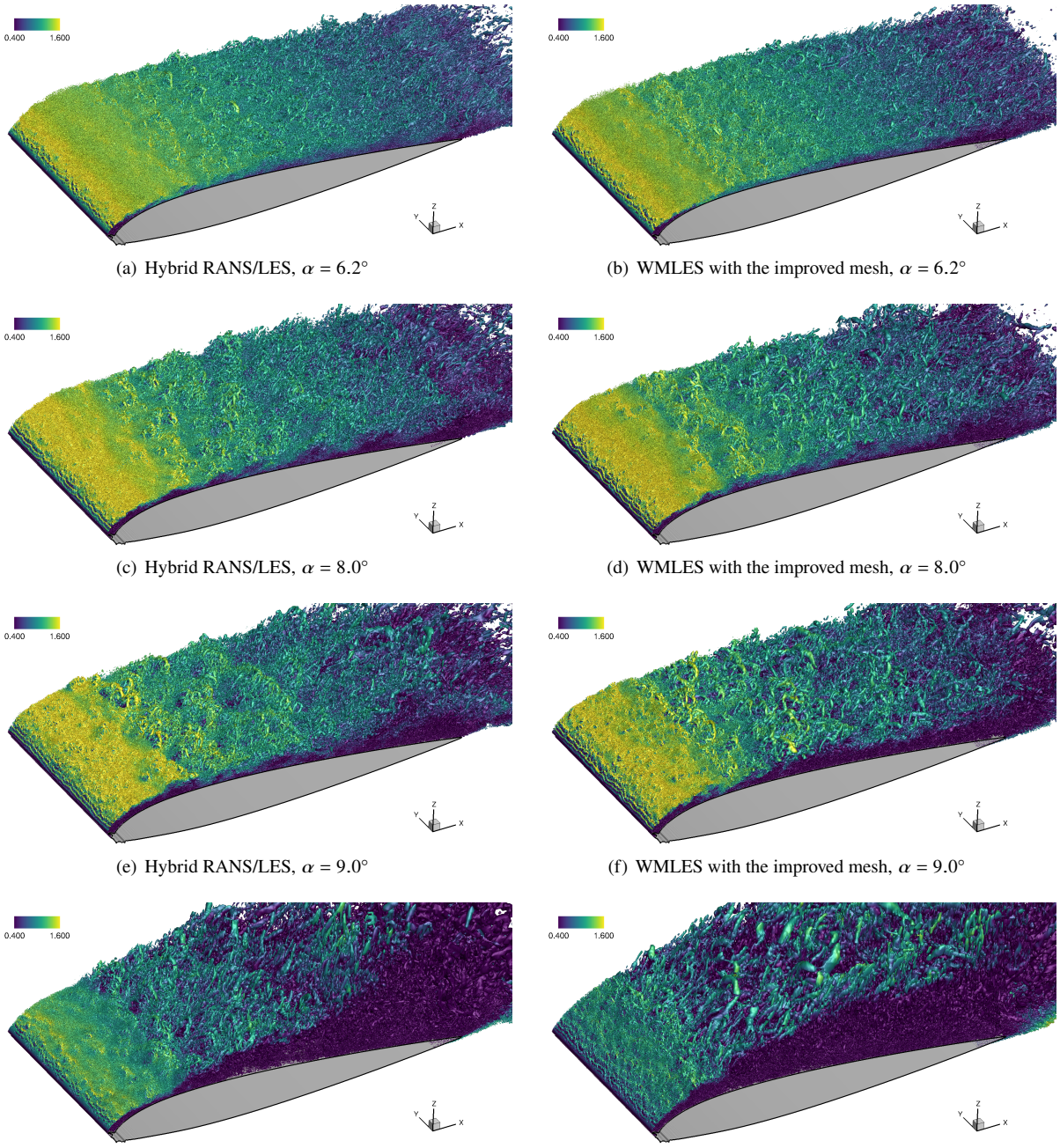

(a) Hybrid RANS/LES, $\alpha = 6.2°$

(b) WMLES with the improved mesh, $\alpha = 6.2°$

(c) Hybrid RANS/LES, $\alpha = 8.0°$

(d) WMLES with the improved mesh, $\alpha = 8.0°$

(e) Hybrid RANS/LES, $\alpha = 9.0°$

(f) WMLES with the improved mesh, $\alpha = 9.0°$

(g) Hybrid RANS/LES, $\alpha = 10.0°$

(h) WMLES with the improved mesh, $\alpha = 10.0°$

Fig. 5 Iso-surfaces of instantaneous Q-criterion normalized by the free-stream velocity magnitude, U_∞, and chord length, c, at the value of 1000. The iso-surfaces are colored by the normalized streamwise (x-) velocity component, u/U_∞, on the top surface of the airfoil.

and free-stream density respectively. The pressure coefficients are also averaged in the spanwise direction in addition to time averaging. The two sets of experimental data at the subscale and full-scale Reynolds numbers are again provided in the plots. While the C_p curves from the two experimental cases are very similar to each other at the same angle of attack, those at the subscale Reynolds number should be used as the reference solutions for the numerical simulations. From Figure 10(a), it can be seen that there are severe adverse pressure gradients caused by the rapid acceleration of the flows around the tip of the upper ice horn for both experiments at $\alpha = 6.2°$ on the upper surface (suction side).

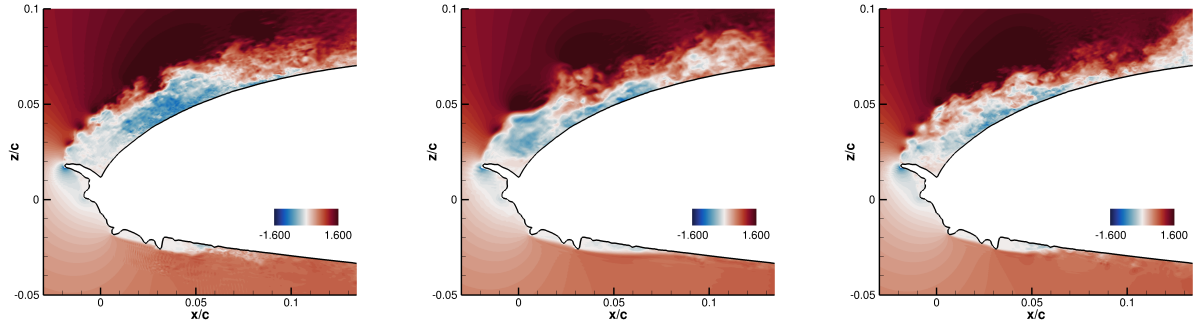

(a) Hybrid RANS/LES (b) WMLES with baseline mesh (c) WMLES with the improved mesh

Fig. 6 Instantaneous streamwise (x-) velocity component, u, normalized by the free-stream velocity magnitude, U_∞, at $\alpha = 8.0°$ from different simulation cases.

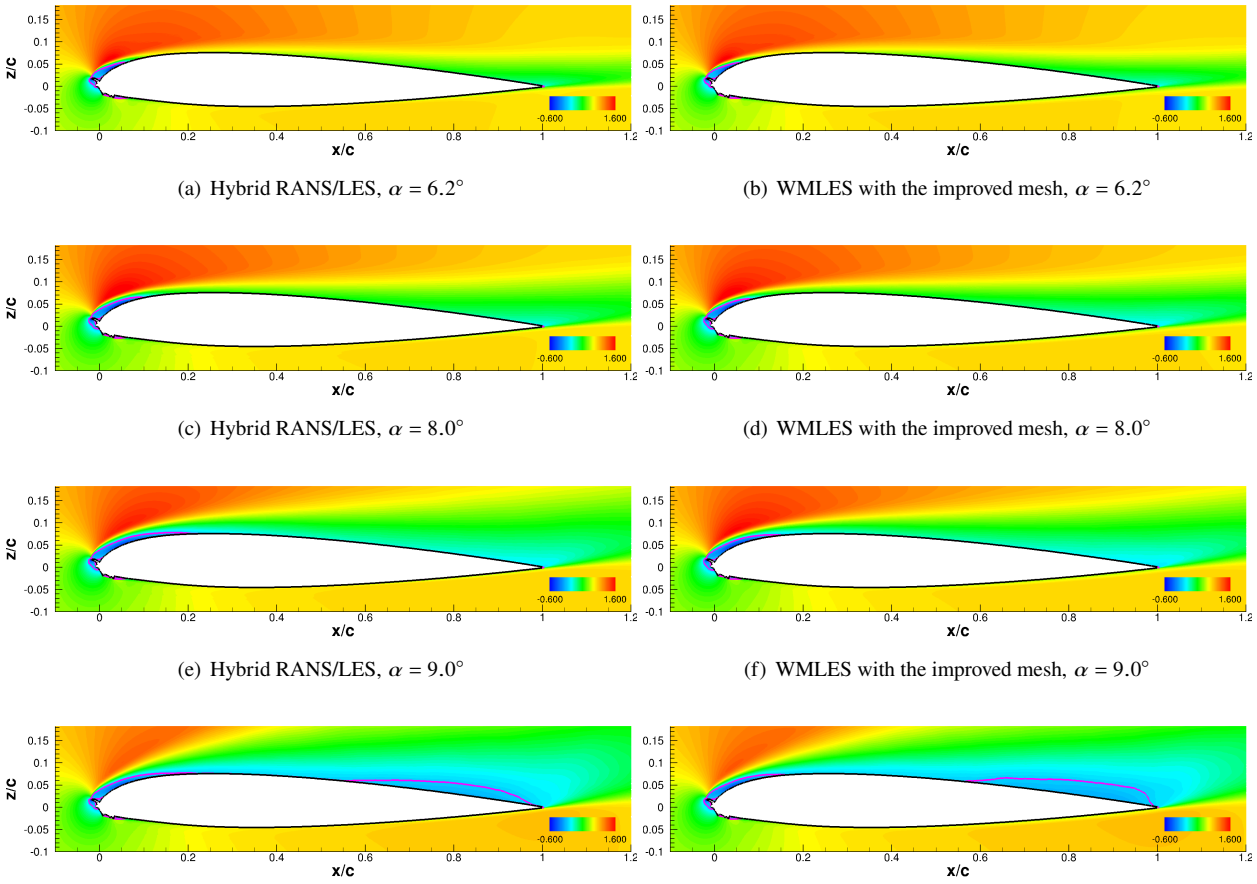

(a) Hybrid RANS/LES, $\alpha = 6.2°$ (b) WMLES with the improved mesh, $\alpha = 6.2°$

(c) Hybrid RANS/LES, $\alpha = 8.0°$ (d) WMLES with the improved mesh, $\alpha = 8.0°$

(e) Hybrid RANS/LES, $\alpha = 9.0°$ (f) WMLES with the improved mesh, $\alpha = 9.0°$

(g) Hybrid RANS/LES, $\alpha = 10.0°$ (h) WMLES with the improved mesh, $\alpha = 10.0°$

Fig. 7 Mean streamwise (x-) velocity component, $\overline{u}$, normalized by the free-stream velocity magnitude, U_∞, from hybrid RANS/LES run and WMLES run with the improved mesh at different angles of attack. The magenta contour lines highlight locations with zero mean velocity component.

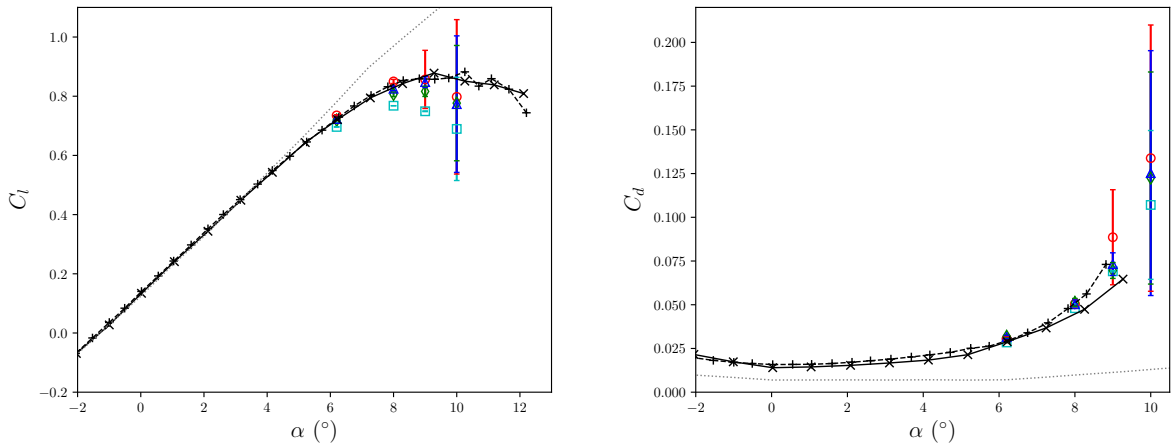

(a) Lift coefficients

(b) Drag coefficients

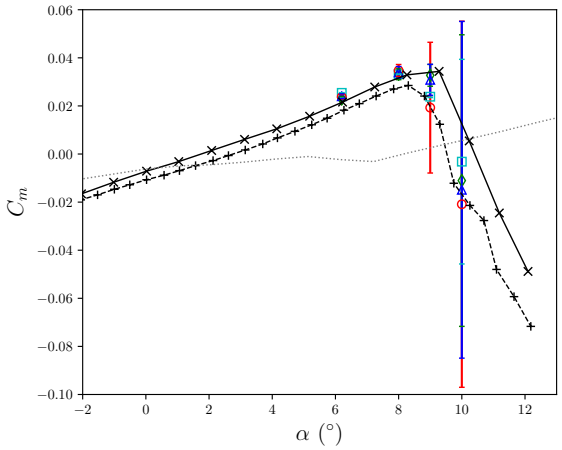

(c) Pitching moment coefficients

Fig. 8 Comparison of lift, drag, and pitching moment coefficients from simulations of iced airfoil at subscale Reynolds number with experimental results. Cyan squares: unsteady RANS; red circles: hybrid RANS/LES; green diamonds: WMLES with baseline grid; blue triangles: WMLES with improved grid; black solid line with crosses: experiment at subscale Reynolds number; black dashed line with pluses: experiment at full-scale Reynolds number; gray dotted line: experiment of clean NACA23012 at subscale Reynolds number. The error bars of the simulation results represent the root mean squares (RMSs) of the aerodynamic coefficients.

There is also a small region near the leading edge with relatively constant pressure on the suction side because of the presence of the separation bubble for each of the experimental cases. Further downstream of the pressure plateau, rapid pressure recovery is observed inside the separation bubble at this angle of attack. The C_p distributions from the hybrid RANS/LES and WMLES runs agree well with the subscale experimental results in the region containing the separation bubble on the upper surface. Moreover, the location of pressure recovery is accurately predicted by all scale-resolving simulations. With grid refinement around the horn ice and the leading edge, the prediction of the magnitude of C_p in the localized low pressure region is also improved for the WMLES. The pressure coefficient distributions obtained with the calculations using the hybrid RANS/LES and the WMLES with the improved mesh are almost identical at this angle of attack. After the pressure recovery, a small negative bump in C_p for the subscale case is not well captured by the

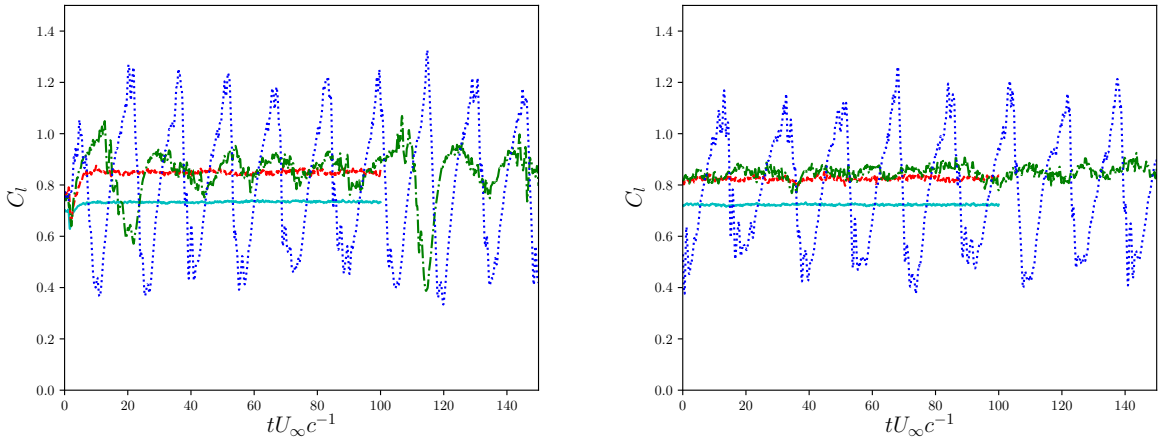

(a) Hybrid RANS/LES

(b) WMLES with the improved mesh

Fig. 9 Time histories of lift coefficients from the hybrid RANS/LES and WMLES runs at different angles of attack α. Cyan solid line: $\alpha = 6.2°$; red dashed line: $\alpha = 8.0°$; green dash-dotted line: $\alpha = 9.0°$; blue dotted line: $\alpha = 10.0°$.

scale-resolving simulations. These simulation results surprisingly agree better with the full-scale case rather than the subscale case after the pressure recovery until the trailing edge although the difference between the two curves from the experiments is small. On the lower surface (pressure side) of the airfoil, the flow remains quite laminar despite flow separation at the lower ice horn. The C_p distributions from the simulations agree well with the experimental results in general. The comparison between the numerical and experimental C_p distributions at another angle of attack, $\alpha = 8.0°$, is shown in Figure 10(b). The two experimental C_p curves are again quite similar except around the separation bubble region. The subscale case has more negative pressure plateau immediately downstream of the tip of the upper horn and faster pressure recovery compared to the full-scale case. This indicates that the separation bubble of the subscale case is smaller than that of the full-scale case. The separation bubble of the case at $\alpha = 8.0°$ is also likely to be larger than that at $\alpha = 6.2°$ for each Reynolds number case as the former has a more gentle pressure recovery. At $\alpha = 8.0°$, the C_p distributions of the hybrid RANS/LES and WMLES runs are quite similar on the upper surface and are essentially the same on the lower surface. The C_p distributions from the simulations have good comparison with the subscale experimental C_p distribution except around the pressure plateau. In this region, the magnitudes of the plateaus fall between the subscale and full-scale experimental values for all of the simulation cases. Comparing the two WMLES results, the WMLES with the improved mesh has slight improvement on the prediction of the magnitude of the pressure plateau compared to that with the baseline mesh. The comparison of C_p distributions at different angles of attack from the simulations using the hybrid RANS/LES and the WMLES with the improved mesh is shown in Figure 11. There is a general trend of decreasing magnitude of the pressure plateau and more gentle pressure recovery downstream of the pressure plateau as the angle of attack increases. This phenomenon is caused by the increase of separation bubble size with the angle of attack, which is indicated by the separation contour lines with zero mean streamwise velocity component on the upper airfoil surface in Figure 7. The curve of the hybrid RANS/LES run on the suction side has a less negative pressure plateau at $\alpha = 9.0°$ compared to that of the WMLES run and this explains why the pitching moment coefficient is smaller and has larger discrepancy compared with the experimental value for the former at this angle of attack.

VII. Turbulent Statistics and Coherent Structures

The turbulent kinetic energy, TKE, and the Reynolds stress tensor, R_{ij}, are studied using the results from the hybrid RANS/LES and the WMLES with the improved mesh. The Reynold stress tensor and TKE are defined as

$$R_{ij} = \overline{u_i' u_j'}, \quad \text{TKE} = \frac{1}{2} R_{kk}, \tag{1}$$

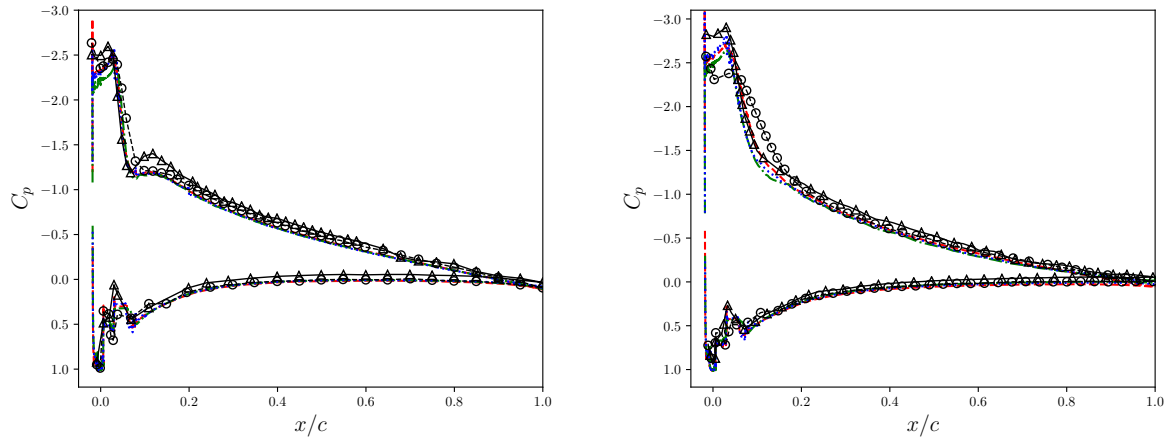

(a) $\alpha = 6.2°$ (b) $\alpha = 8.0°$

Fig. 10 Comparison of mean surface pressure coefficients, C_p, from different simulations of iced airfoil at subscale Reynolds number at two different angles of attack $\alpha = 6.2°$ and $\alpha = 8.0°$. Red dashed line: hybrid RANS/LES; green dash-dotted line: WMLES with baseline grid; blue dotted line: WMLES with the improved mesh; black solid line with triangles: experiment at subscale Reynolds number; black dashed line with circles: experiment at full-scale Reynolds number.

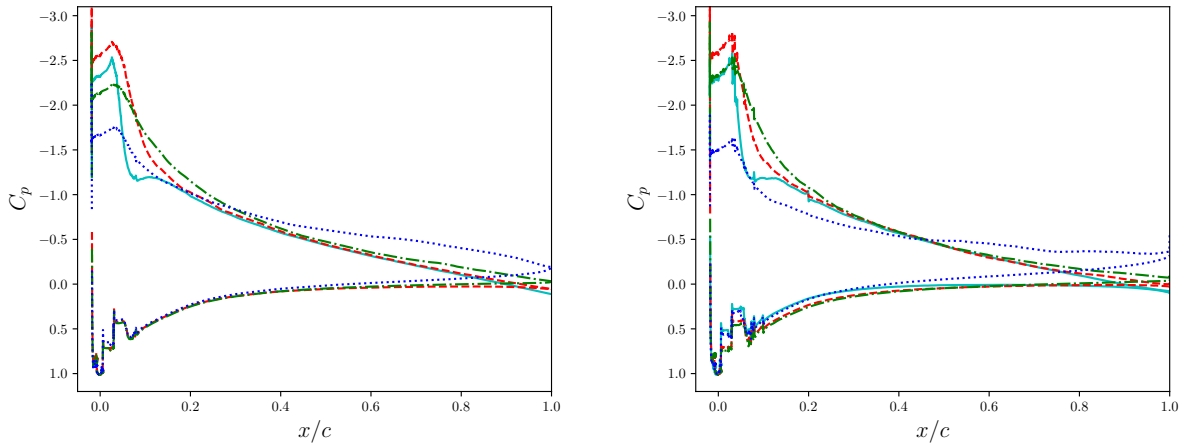

(a) Hybrid RANS/LES (b) WMLES with the improved mesh

Fig. 11 Mean surface pressure coefficients, C_p, from hybrid RANS/LES run and WMLES run with the improved mesh at different angles of attack α. Cyan solid line: $\alpha = 6.2°$; red dashed line: $\alpha = 8.0°$; green dash-dotted line: $\alpha = 9.0°$; blue dotted line: $\alpha = 10.0°$.

where $u_i = [u_1\ u_2\ u_3]^T = [u\ v\ w]^T$ represents the velocity vector and $u_i' = u_i - \overline{u}_i$ is the fluctuation of the velocity. The contours of normalized turbulent kinetic energy, TKE/U_∞^2, from the hybrid RANS/LES and the WMLES with the improved mesh on a x-z plane are shown in Figure 12. From these plots, it is shown that the peaks of TKE contours from different angles of attack are all at locations shortly downstream of the upper ice horn tip and the peak values are quite independent of the angle of attack. These regions of highly turbulent flows are the results of the rapid transition to turbulence caused by the KHI at the shear layers induced by the horn ice tip. At the lower angles of attack such as

$\alpha = 6.2^\circ$ and $\alpha = 8.0^\circ$, the TKE magnitudes of the turbulent flows remain high for a quite long distance downstream of the horn ice on the upper surface of the airfoil, different than flows on regular clean airfoils. As the angle of attack increases, there is a wider spread of high TKE with larger thickness on the upper surface of the airfoil and this indicates more turbulent flow induced by the horn ice. At the post-stall angle of attack $\alpha = 10.0^\circ$, it can be seen that the entire upper surface of the airfoil is covered by highly turbulent flow and the TKE value at the trailing edge is around five times more than that at $\alpha = 6.2^\circ$. The TKE contours from the hybrid RANS/LES and the WMLES with the improved mesh are basically the same at each angle of attack, except at $\alpha = 9.0^\circ$ where small difference in the contours is noticed. At this angle of attack that is close to stall, there is a slightly larger region of high TKE on the airfoil from the hybrid RANS/LES results compared to the WMLES results. This wider spread of high TKE in the vertical direction predicted from hybrid RANS/LES is consistent with larger fluctuation observed on the C_l and other aerodynamic coefficients from the hybrid RANS/LES compared to the WMLES. The anisotropy of the Reynolds stress tensor is also studied and it is defined as $b_{ij} = R_{ij}/R_{kk} - \delta_{ij}/3$, where δ_{ij} is the Kronecker delta. The diagonal components of the anisotropy tensor have values between -1/3 and 2/3. The former and latter limits for any Reynolds normal stress component represent no and full contributions respectively from that component to the TKE. The anisotropy of the Reynolds normal stress components obtained with the simulations of hybrid RANS/LES and WMLES using the improved mesh at $\alpha = 8.0^\circ$ and $\alpha = 10.0^\circ$ are shown in Figures 13 and 14 respectively. Note that the Reynolds normal stress components are isotropic if $b_{11} = b_{22} = b_{33} = 0$ (white color with the chosen color map in the figures). As seen from the figures, the results from the hybrid RANS/LES and WMLES are very close to each other at the same angle of attack and the Reynolds normal stress on the upper airfoil surface is very anisotropic. The streamwise Reynolds stress component R_{11} is the main contributor to the TKE at both angles of attack. At $\alpha = 8.0^\circ$, the spanwise component R_{22} is larger than the vertical component R_{33}. However, both components become smaller and closer to each other at the post-stall angle $\alpha = 10.0^\circ$ as R_{11} becomes even more dominant in TKE.

In order to extract any coherent structures of the flows around the iced airfoil that are caused by the unstable hydrodynamic modes at the shear layers, the spectral proper orthogonal decomposition (SPOD) post-processing method is employed. The SPOD is a special form of the more popular "standard" proper orthogonal decomposition (POD) method which was introduced as a data-driven approach to the community of fluid mechanics by Lumley [50]. In this approach, POD modes are extracted using the two-point spatial correlation tensor based on the chosen definition of energy norm or inner product. These POD modes are the most optimal modes in which a subset of the modes can reconstruct a large portion of the energy defined by the inner product. The spectral POD, or SPOD is different from the "standard" POD as the former has a space-time decomposition under the assumption that the flow data is statistically stationary while the latter only considers correlation in space and not the sequential ordering of data in time. As a result, the SPOD can extract modes that are both coherent in space and time while the "standard" POD only gives spatially coherent modes [51]. While the SPOD is re-introduced recently [51, 52], much of the original literature of it stems from the early works by Lumley [50, 53].

The procedure of the SPOD data analysis method is first briefly explained. We define the primitive variable vector as $\boldsymbol{q}(\boldsymbol{x}, t) = [p\ u\ v\ w]^T$ that is a function of location vector, $\boldsymbol{x}$, and time, t. In this work, we seek SPOD modes that are optimal in terms of the following space-time inner product between any two primitive variable vectors $\boldsymbol{q}_i$ and $\boldsymbol{q}_j$ at different $\boldsymbol{x}$ and t:

$$\left\langle \boldsymbol{q}_i, \boldsymbol{q}_j \right\rangle = \int_{-\infty}^{\infty} \int_{-L/2}^{L/2} \int_A \left(p_i \sigma_p {p_j}^* + u_i \sigma_u {u_j}^* + v_i \sigma_v {v_j}^* + w_i \sigma_w {w_j}^* \right) dA\ dy\ dt, \tag{2}$$

where A is the 2D sampling domain on the x-z plane chosen for the SPOD post-processing and $L = 0.5c$ is the computational domain width in the spanwise direction. The weighting vector is given by $\boldsymbol{\sigma} = \left[\sigma_p\ \sigma_u\ \sigma_v\ \sigma_w\right]^T$. The pressure and turbulent kinetic energy (TKE) norms are retrieved when $\boldsymbol{\sigma} = [1\ 0\ 0\ 0]^T$ and $\boldsymbol{\sigma} = [0\ 1\ 1\ 1]^T$ respectively. Since the data is statistically stationary and homogeneous in the spanwise direction, y-direction, it is convenient to solve the SPOD eigenvalue problem with a two-point correlation matrix, the cross-spectral density (CSD) matrix, that is Fourier transformed in both time and spanwise spatial direction. To construct the ensemble of realizations from a single and long time series, the Welch method is used to partition the data in time with overlapping blocks/realizations and a 50% overlap is used in this work. To reduce spectral leakage, the Hann window function is applied to each block/realization before taking Fourier transform in time. After the partitioning of data into n_{blk} blocks in time and applying Fourier transformation on each block, we have the Fourier transformed data matrix at l-th frequency in time and m-th mode number in the spanwise direction:

$$\hat{\boldsymbol{Q}}_{l,m} = \left[\hat{\boldsymbol{q}}_{l,m}^{(1)}, \hat{\boldsymbol{q}}_{l,m}^{(2)}, \cdots, \hat{\boldsymbol{q}}_{l,m}^{(n_{blk})} \right], \tag{3}$$

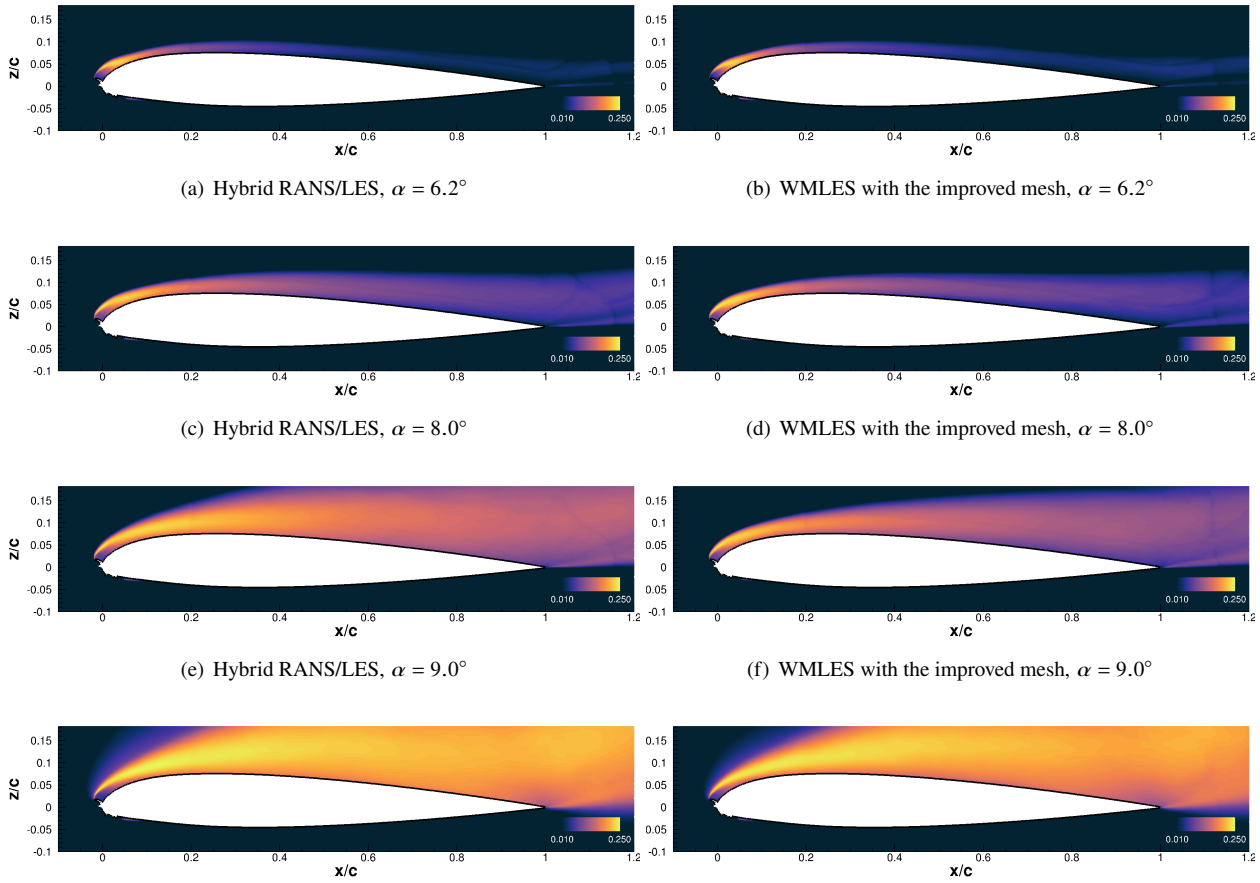

(a) Hybrid RANS/LES, $\alpha = 6.2°$

(b) WMLES with the improved mesh, $\alpha = 6.2°$

(c) Hybrid RANS/LES, $\alpha = 8.0°$

(d) WMLES with the improved mesh, $\alpha = 8.0°$

(e) Hybrid RANS/LES, $\alpha = 9.0°$

(f) WMLES with the improved mesh, $\alpha = 9.0°$

(g) Hybrid RANS/LES, $\alpha = 10.0°$

(h) WMLES with the improved mesh, $\alpha = 10.0°$

Fig. 12 Turbulent kinetic energy, TKE, normalized by the free-stream velocity magnitude, U_∞, from the hybrid RANS/LES and the WMLES with the improved mesh at different angles of attack.

where $\hat{\boldsymbol{q}}_{l,m}^{(k)}$ is the k-th Fourier realization at l-th frequency and m-th spanwise mode number. Note that a spanwise mode number of m means a wavenumber of m/L and should not be confused with the SPOD mode number. It should also be noted that the multi-dimensional data of $\boldsymbol{q}$ at a time t and a spanwise location y, which is discretized in a 2D sampling domain with $n_x \times n_z$ points, is first stacked into a single vector of size $4 \times n_x \times n_z$ before the Fourier transformation is applied. While the SPOD mode energy represented by the eigenvalue, $\lambda_{l,m}$, and the SPOD mode eigenvector, $\boldsymbol{\phi}_{l,m}$, at each combination of frequency and spanwise mode number can be computed from the CSD matrix, $\hat{\boldsymbol{Q}}_{l,m}\hat{\boldsymbol{Q}}_{l,m}^*$, with the weight matrix $\boldsymbol{W}$ derived with $\boldsymbol{\sigma}$, it is computationally more efficient to solve the following analogous eigenvalue: problem [51, 52, 54]

$$\frac{1}{n_{blk}}\hat{\boldsymbol{Q}}_{l,m}^*\boldsymbol{W}\hat{\boldsymbol{Q}}_{l,m}\boldsymbol{\Psi}_{l,m} = \boldsymbol{\Psi}_{l,m}\boldsymbol{\Lambda}_{l,m}. \tag{4}$$

The SPOD modes at l-th frequency and m-th spanwise mode number can be reconstructed from

$$\boldsymbol{\Phi}_{l,m} = \frac{1}{\sqrt{n_{blk}}}\hat{\boldsymbol{Q}}_{l,m}\boldsymbol{\Psi}_{l,m}\boldsymbol{\Lambda}_{l,m}^{-1/2}. \tag{5}$$

The elements along the diagonal of the diagonal matrix $\boldsymbol{\Lambda}_{l,m}$ are the sorted eigenvalues $\lambda_{l,m}^{(1)} \geq \lambda_{l,m}^{(2)} \geq \cdots \geq \lambda_{l,m}^{(n_{blk})}$ and $\boldsymbol{\Phi}_{l,m} = \left[\boldsymbol{\phi}_{l,m}^{(1)}, \boldsymbol{\phi}_{l,m}^{(2)}, \cdots, \boldsymbol{\phi}_{l,m}^{(n_{blk})}\right]$ is the corresponding eigenvector matrix.

20 CTUs of time-resolved data from the WMLES calculations with the improved mesh are used for the SPOD analysis at different angles of attack. The data is collected in a box with full span around the leading edge of the iced

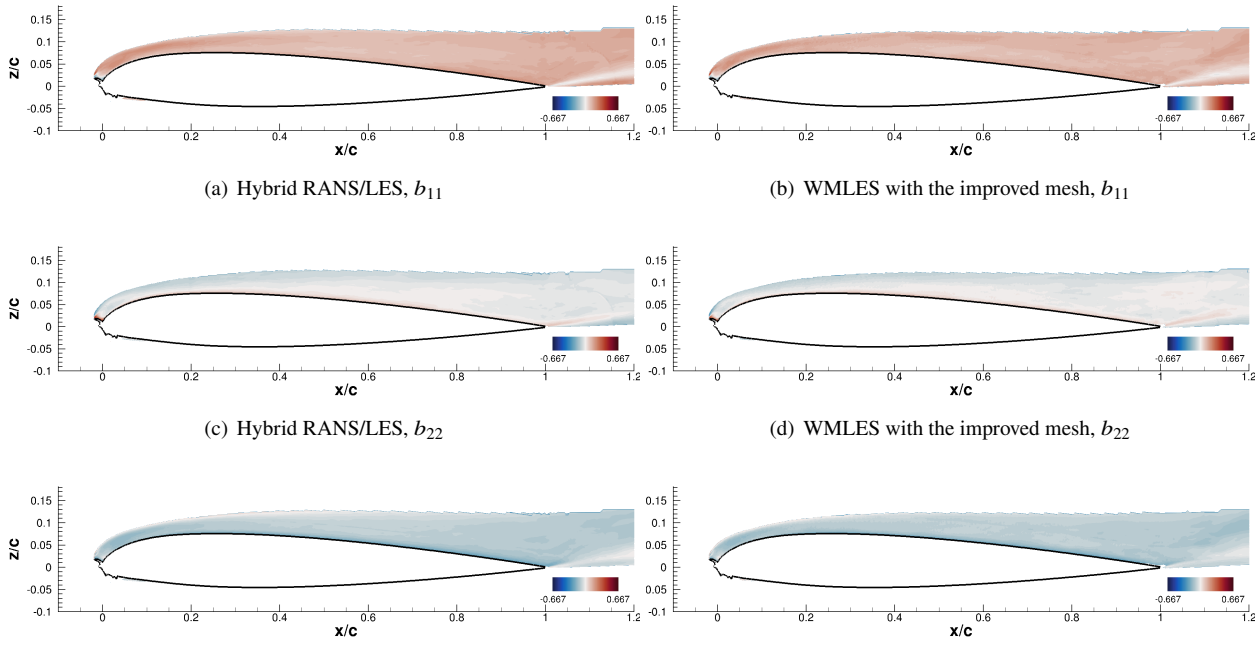

(a) Hybrid RANS/LES, b_{11}

(b) WMLES with the improved mesh, b_{11}

(c) Hybrid RANS/LES, b_{22}

(d) WMLES with the improved mesh, b_{22}

(e) Hybrid RANS/LES, b_{33}

(f) WMLES with the improved mesh, b_{33}

Fig. 13 Anisotropy of Reynolds normal stress components from the hybrid RANS/LES and the WMLES with the improved mesh at angle of attack $\alpha = 8.0°$. The regions with normalized turbulent kinetic energy, TKE/U_∞^2, smaller than 0.01 are masked.

airfoil with a sampling rate of 1000 3D snapshots per CTU. Figure 15 shows the eigenvalues of the SPOD modes based on the pressure and TKE norms at different frequencies and spanwise mode number $m = 0$, i.e. no variation in the spanwise direction, at $\alpha = 8°$. From both plots, it can be seen that there are five distinct peaks for the leading order SPOD mode based on the two different definitions of energy norm. The five peaks are at the Strouhal numbers of $St = 31.5$, 48.3, 96.6 147.1, and 195.9. The Strouhal numbers are defined as frequencies f normalized with the free-stream velocity magnitude and the chord length, i.e. $St = fcU_\infty^{-1}$. At each of these five Strouhal numbers and $m = 0$, low order behaviour is observed as the leading order SPOD mode has much larger energy compared to the other modes and the low order behaviour is stronger for peaks at lower Strouhal numbers. From the eigenvectors, we have identified the leading order modes at $St = 31.5$ and $St = 48.3$ as the coherent structures in the shear layers induced by the lower and upper horns respectively. The leading order SPOD modes at the other three higher Strouhal numbers are the harmonics of the SPOD mode at the fundamental Strouhal number $St = 48.3$. The real parts of the eigenvectors at $St = 48.3$ and its harmonic Strouhal numbers based on the pressure norm are shown in Figure 16. These eigenvectors have large magnitudes along the location of the shear layer as these SPOD modes represent the instability modes of the KHI generated at the shear layer. The oscillating mode has a smaller wavelength and is more localized towards the tip of the horn ice as the Strouhal number increases. In Figure 17, the eigenvalues of the leading order SPOD modes at different spanwise mode numbers m are compared. It can be seen that there are also peaks in the leading order modes at the same set of Strouhal numbers when the spanwise mode number or wavenumber is low except at $St = 31.5$,. This indicates that the KHI modes also have low fluctuations in the spanwise direction and this is consistent with the low wavenumber fluctuations of the rolled-up vortices observed on the Q-criterion iso-surfaces immediately downstream of the upper ice horn in Figure 5. Figure 18 compares the u, v, and w components of the real parts of the leading SPOD modes based on the TKE norm with that based on the pressure norm at different spanwise mode numbers but at the same fundamental Strouhal number $St = 48.3$. At $m = 0$, the spanwise velocity component v of the eigenvector should theoretically be zero. While the magnitude of this component is not statistically converged to zero from the plot, it is at least one order of magnitude smaller than those of another two velocity components. Other velocity components of the SPOD mode based on TKE norm have magnitudes and wavelengths similar to the SPOD mode based on pressure norm at $m = 0$. As the spanwise mode number increases, the magnitude of the spanwise velocity component increases and

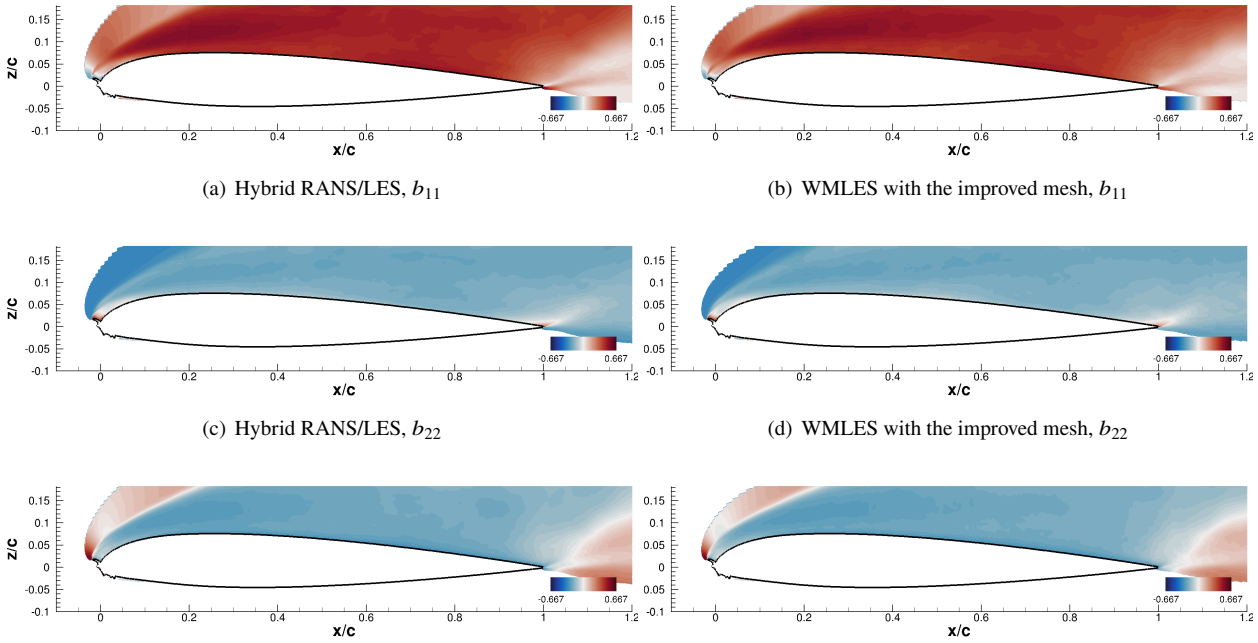

(a) Hybrid RANS/LES, b_{11}

(b) WMLES with the improved mesh, b_{11}

(c) Hybrid RANS/LES, b_{22}

(d) WMLES with the improved mesh, b_{22}

(e) Hybrid RANS/LES, b_{33}

(f) WMLES with the improved mesh, b_{33}

Fig. 14 Anisotropy of Reynolds normal stress components from the hybrid RANS/LES and the WMLES with the improved mesh at angle of attack $\alpha = 10.0°$. The regions with normalized turbulent kinetic energy, TKE/U_∞^2, smaller than 0.01 are masked.

becomes comparable to other velocity components at $m = 8$. As for other velocity components based on the TKE norm and the pressure component based on pressure norm, their magnitudes and the wavelengths remain quite unchanged with the change in the spanwise mode number.

The eigenvalues of the leading order SPOD modes at $m = 0$ and different angles of attack are compared in Figure 19. From the figure, we can also identify distinct peaks of the SPOD modes at angles of attack other than $\alpha = 8.0°$ based on both pressure and TKE norms. Interestingly, no distinct peaks or coherent structures corresponding to any KHI induced by the upper ice horn are identified at $\alpha = 6.2°$. At the higher angles of attack, the fundamental Strouhal number related to the KHI at the shear layer induced by the upper ice horn is essentially independent of the angle of attack and the value is at around $St = 48$. Nevertheless, the Strouhal number of the KHI induced by the lower ice horn reduces as the angle of attack increases and the Strouhal numbers at $\alpha = 6.2°$, $\alpha = 8.0°$, $\alpha = 9.0°$, and $\alpha = 10.0°$ are $St = 36.2$, 31.5, 31.0, and 27.3 respectively. Figures 20 and 21 compare the real parts of the leading order SPOD eigenvectors at $m = 0$ and different angles of attack based on the pressure norm at the fundamental Strouhal numbers corresponding to the lower and upper instabilities respectively. It is shown that as the angle of attack increases, the propagation direction of the lower horn KHI leading order mode remains relatively unchanged but the wavelength increases gradually. The wavelength of the SPOD mode for the upper horn KHI remains constant with the angle of attack (except at $\alpha = 6.2°$ where the KHI mode is missing) but the mode propagates at a more inclined angle relative to the airfoil chord line as the angle of attack increases.

VIII. Concluding Remarks

The flows around an airfoil with horn ice accretion were simulated with two different turbulence approaches, the hybrid RANS/LES and WMLES, using body-fitted curvilinear meshes coupled with the penalty immersed boundary method, at four different angles of attack from pre-stall to post-stall regimes. In these simulations with the hybrid BF/IB approach, the effects of the ice accreted at the leading edge of the airfoil were successfully imposed using source terms while the flows around the clean portion of the airfoil surface were handled with the more mature boundary treatments, which are the hybrid RANS/LES using the ZDES mode 2 with EP and the WMLES using the algebraic wall model in

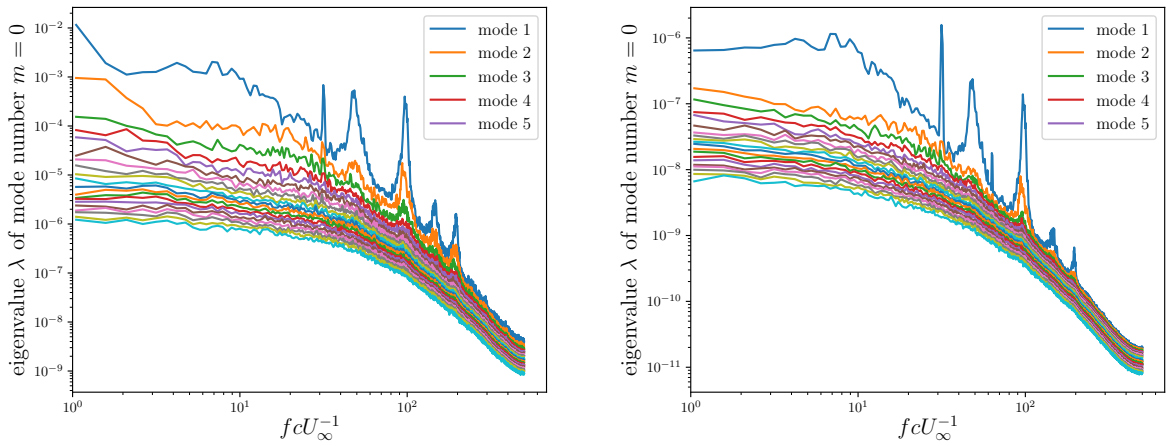

(a) Pressure norm

(b) TKE norm

Fig. 15 The eigenvalues λ of the SPOD modes at spanwise mode number $m = 0$ computed with the pressure norm and turbulent kinetic energy (TKE) norm at angle of attack $\alpha = 8°$. The modes are sorted in descending order of the energy given by the eigenvalues at each frequency.

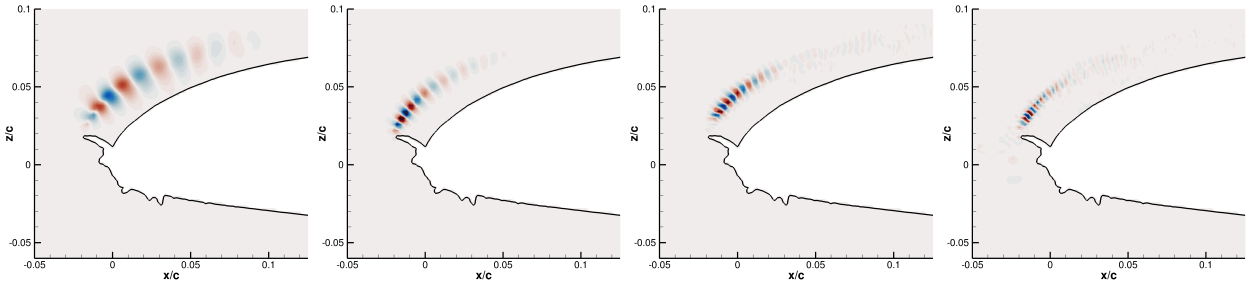

(a) $St = 48.3$ (b) $St = 96.6$ (c) $St = 147.1$ (d) $St = 195.9$

Fig. 16 The real parts of the leading SPOD modes at spanwise mode number $m = 0$ based on the pressure norm at the Strouhal numbers, $St = fcU_\infty^{-1}$, for the Kelvin–Helmholtz instability (KHI) induced by the upper ice horn at angle of attack $\alpha = 8.0°$.

this work. Due to the differences in the numerical methods and turbulence modeling between the hybrid RANS/LES and WMLES approaches, different meshes were designed for the simulations. The hybrid RANS/LES requires unit normalized wall distance at the first cell node, resulting highly anisotropic cells at the wall while the WMLES requires more isotropic cells near wall in practice. The implicit time stepping used with the hybrid RANS/LES allows larger time step compared with the WMLES where the acoustic CFL constraints are required to be met. The time scale of the penalty source terms used in the immersed boundary method can also be much smaller than the time step size for the hybrid RANS/LES while the WMLES requires the time scale to be larger than the explicit time step size due to the stability reason.

It was found that the aerodynamic loads and pitching moments from the hybrid RANS/LES and WMLES calculations have good agreements with the experimental results at low angles of attack, such as $\alpha = 6.2°$ and $\alpha = 8.0°$. At these two angles of attack, grid sensitivity was shown for the WMLES runs with two different mesh resolutions near the iced leading edge and improvements on the pressure plateaus near the leading edge were seen with mesh refinement near the horn ice. At the higher angle of attack $\alpha = 9.0°$, differences in the drag and pitching moment coefficients between the hybrid RANS/LES and WMLES runs were observed. Moreover, the aerodynamic coefficients obtained with the hybrid

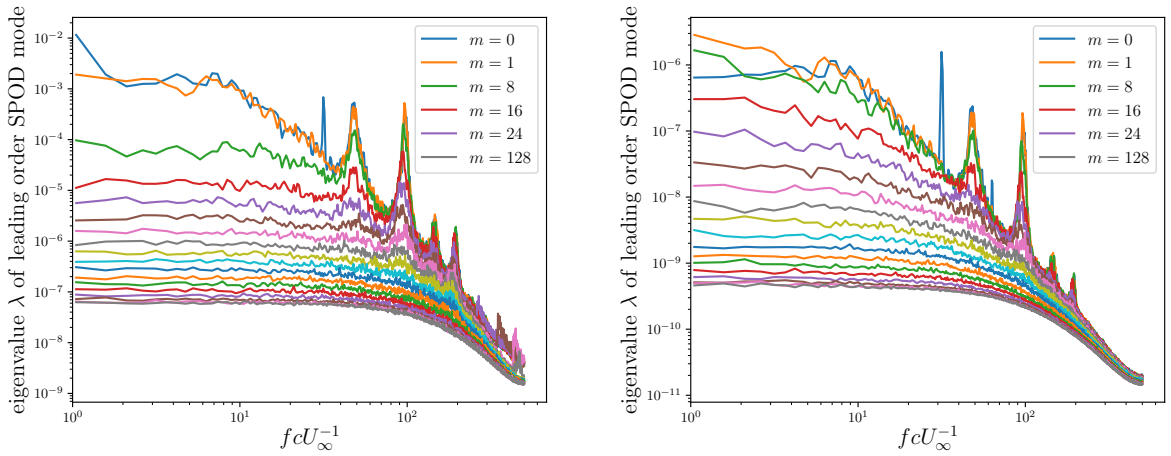

(a) Pressure norm

(b) TKE norm

Fig. 17 The eigenvalues λ of the leading SPOD modes at different spanwise mode numbers m computed with the pressure norm and turbulent kinetic energy (TKE) norm at angle of attack $\alpha = 8.0°$.

RANS/LES computation have larger fluctuations compared to those from the WMLES runs. At this angle of attack, the drag and moment coefficients obtained from the WMLES runs agree better with the experimental results, although the lift coefficients from both the hybrid RANS/LES and the WMLES with the improved mesh simulations are very close to each other and agree well with the experimental value. Larger discrepancies between the simulation and experimental results were seen at the post-stall angle of attack $\alpha = 10.0°$ despite very large variations in the aerodynamic quantities.

The TKE and the Reynolds normal stress components were also studied at different angles of attack. At the lowest angle of attack $\alpha = 6.2°$, a localized region of large TKE was observed around the shear layer triggered by the upper ice horn. As the angle of attack increases, the region of large TKE spreads downstream and has a larger thickness on the upper surface of the airfoil although the peak of the TKE is still around the location close to the aft of the horn ice and the peak value remains quite unchanged. At the post-stall angle of attack $\alpha = 10.0°$, the flow is highly turbulent on the entire upper surface of the iced airfoil. At low angle of attack, the TKE was observed to be largely composed of the streamwise Reynolds normal stress component while the vertical component contributes the least to the TKE among the three normal stress components. The contribution of streamwise Reynolds normal stress component to TKE rises with the angle of attack and the TKE is mainly composed of the streamwise component at $\alpha = 10.0°$. Finally, the coherent structures at the shear layers induced by the upper and lower ice horns were extracted using the SPOD technique based on the pressure and TKE norms with different mode numbers in the periodic spanwise direction. These SPOD modes were found to have low order behaviour at zero and low spanwise mode numbers, and can be studied mainly through the leading order SPOD modes. A Strouhal number that is related to the KHI modes of the shear layer caused by the lower horn was identified for all four angles of attack studies at zero spanwise mode number. While no clear SPOD modes triggered by the upper ice horn were observed at $\alpha = 6.2°$, SPOD modes at a fundamental Strouhal number with multiple harmonics were successfully extracted at other higher angles of attack when the spanwise mode number is small. It is also found that the magnitude of the spanwise velocity component of the leading SPOD eigenvector based on the TKE norm increases with the spanwise mode number from essentially zero at $m = 0$ and the component becomes comparable to other velocity components when $m = 8$.

Acknowledgments

This work was partially funded by the NASA's Aeronautics Research Mission Directorate's (ARMD) Transformational Tools and Technologies (T^3) and the Advanced Air Transport Technology (AATT) projects. Computer time has been provided by the NASA Advanced Supercomputing (NAS) facility at NASA Ames Research Center. We would like to thank Dr. Jeffrey A. Housman and Dr. Oliver M. Browne of NASA Ames Research Center for the excellent advice on the setup of the RANS and scale-resolving simulations. We also gratefully acknowledge Dr. Andy P. Broeren from

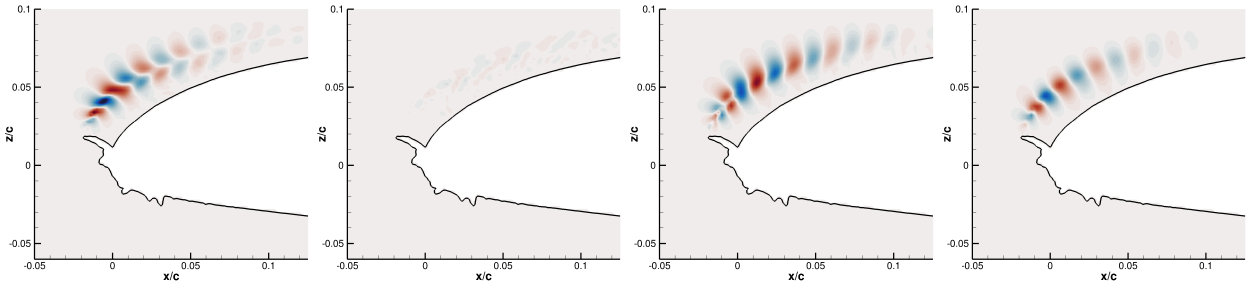

(a) u, $m = 0$ (b) v, $m = 0$ (c) w, $m = 0$ (d) p, $m = 0$

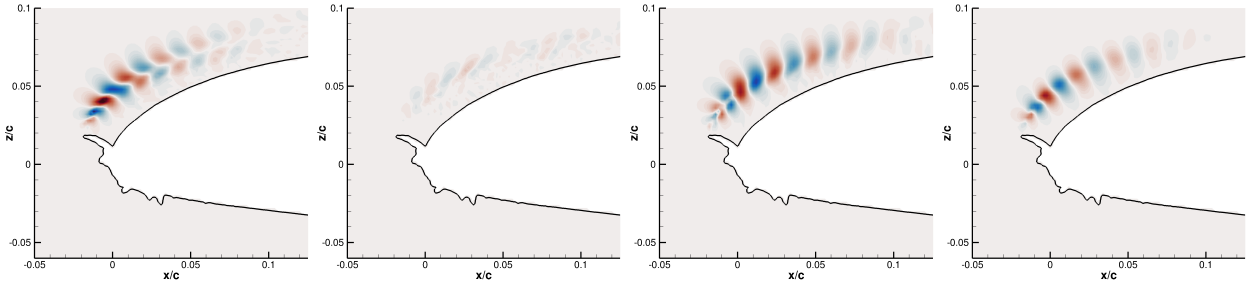

(e) u, $m = 1$ (f) v, $m = 1$ (g) w, $m = 1$ (h) p, $m = 1$

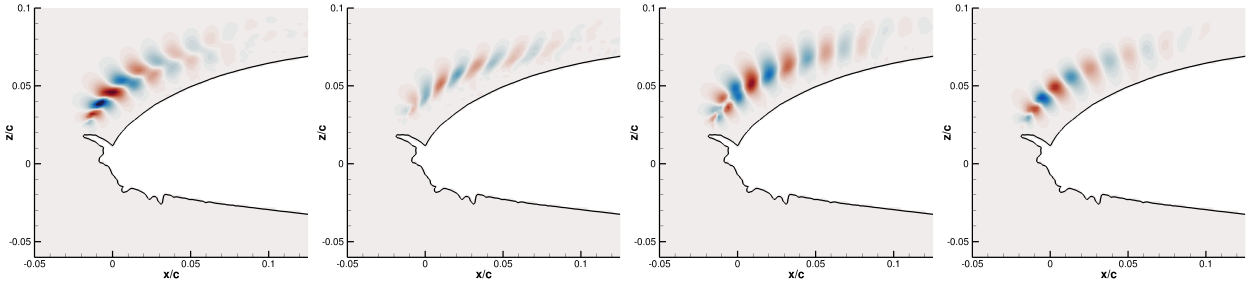

(i) u, $m = 4$ (j) v, $m = 4$ (k) w, $m = 4$ (l) p, $m = 4$

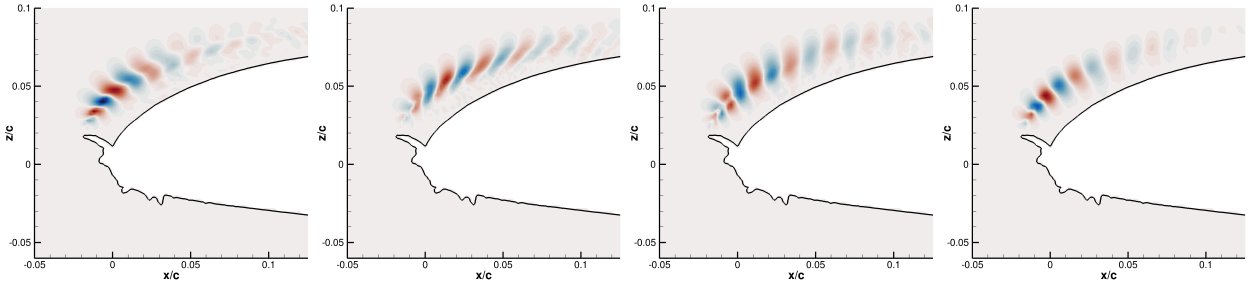

(m) u, $m = 8$ (n) v, $m = 8$ (o) w, $m = 8$ (p) p, $m = 8$

Fig. 18 Comparison of the real parts of different velocity components of the leading SPOD modes at different spanwise mode numbers based on the turbulent kinetic energy (TKE) norm with those based on pressure (p) norm at the fundamental Strouhal number, $St = fcU_\infty^{-1} = 48.3$, for the Kelvin–Helmholtz instability (KHI) induced by the upper ice horn at angle of attack $\alpha = 8.0°$. The three components of the SPOD mode based on the TKE norm are the streamwise velocity component, u, spanwise velocity component, v, and vertical velocity component, w. Note that all plots have the same minimum and maximum limits for the contours.

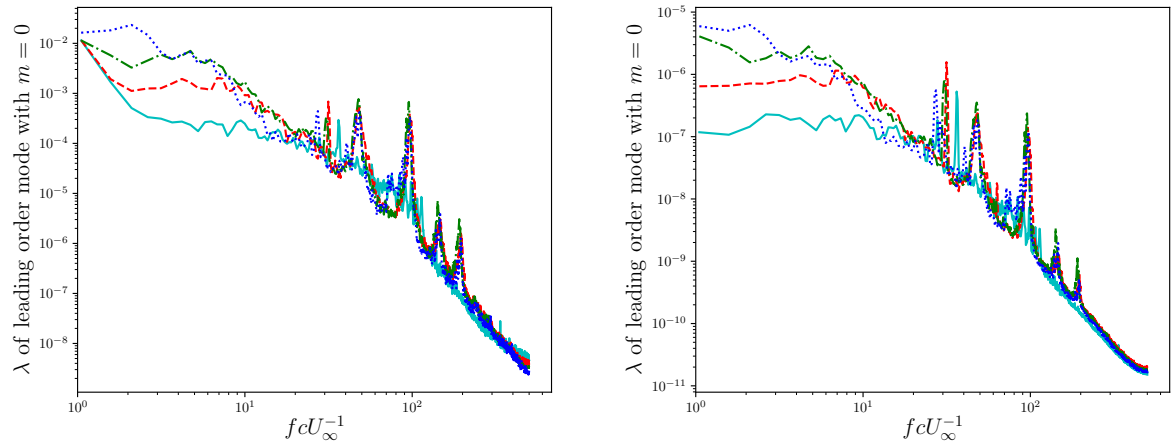

(a) Pressure norm (b) TKE norm

Fig. 19 The eigenvalues λ of the leading SPOD modes at spanwise mode number $m = 0$ based on the pressure norm and turbulent kinetic energy (TKE) norm at different angles of attack α. Cyan solid line: $\alpha = 6.2°$; red dashed line: $\alpha = 8.0°$; green dash-dotted line: $\alpha = 9.0°$; blue dotted line: $\alpha = 10.0°$.

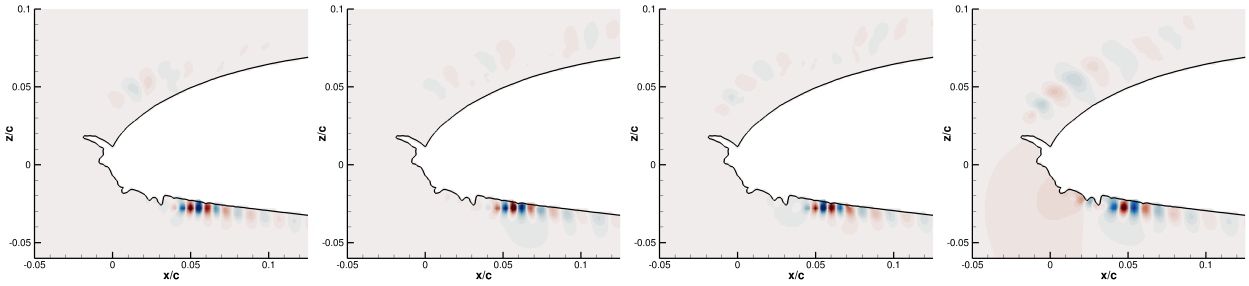

(a) $\alpha = 6.2°$ at $St = 36.2$ (b) $\alpha = 8.0°$ at $St = 31.5$ (c) $\alpha = 9.0°$ at $St = 31.0$ (d) $\alpha = 10.0°$ at $St = 27.3$

Fig. 20 The leading SPOD modes at spanwise mode number $m = 0$ based on the pressure norm at the base Strouhal numbers, $St = fcU_\infty^{-1}$, for the Kelvin–Helmholtz instability (KHI) induced by the lower ice horn at different angles of attack α.

NASA John H. Glenn Research Center for valuable discussions.

References

[1] Bragg, M. B., Broeren, A. P., and Blumenthal, L. A., "Iced-airfoil aerodynamics," *Progress in Aerospace Sciences*, Vol. 41, No. 5, 2005, pp. 323–362.

[2] Leary, W. M., *We Freeze to Please: A History of NASA's Icing Research Tunnel and the Quest for Flight Safety*, Vol. 4226, National Aeronautics and Space Administration, 2002.

[3] Addy, H. E., *Ice accretions and icing effects for modern airfoils*, National Aeronautics Administration, Glenn Research Center, 2000.

[4] Addy, H., Broeren, A., Zoeckler, J., and Lee, S., "A wind tunnel study of icing effects on a business jet airfoil," *41st Aerospace Sciences Meeting and Exhibit*, 2003, p. 727.

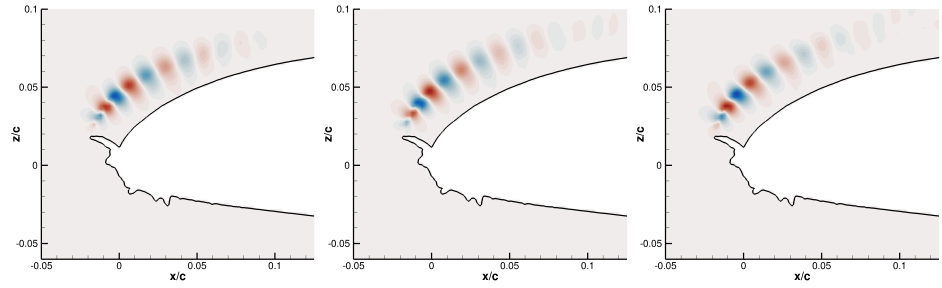

(a) $\alpha = 8.0°$ at $St = 48.3$ (b) $\alpha = 9.0°$ at $St = 47.8$ (c) $\alpha = 10.0°$ at $St = 48.3$

Fig. 21 The leading SPOD modes at spanwise mode number $m = 0$ based on the pressure norm at the base Strouhal numbers, $St = fcU_\infty^{-1}$, for the Kelvin–Helmholtz instability (KHI) induced by the upper ice horn at different angles of attack α.

[5] Bragg, M., Broeren, A., Addy, H., Potapczuk, M., Guffond, D., and Montreuil, E., "Airfoil ice-accretion aerodynamic simulation," *45th AIAA Aerospace Sciences Meeting and Exhibit*, 2007, p. 85.

[6] Broeren, A. P., Bragg, M. B., Addy Jr, H. E., Lee, S., Moens, F., and Guffond, D., "Effect of high-fidelity ice-accretion simulations on full-scale airfoil performance," *Journal of aircraft*, Vol. 47, No. 1, 2010, pp. 240–254.

[7] Lee, S., Ratvasky, T., Thacker, M., and Barnhart, B., "Geometry and Reynolds-number scaling on an iced business-jet wing," *43rd AIAA Aerospace Sciences Meeting and Exhibit*, 2005, p. 1066.

[8] Lee, S., Broeren, A. P., Woodard, B., Lum, C. W., and Smith, T. G., "Comparison of Iced Aerodynamic Measurements on Swept Wing from Two Wind Tunnels," *2018 Atmospheric and Space Environments Conference*, 2018, p. 3493.

[9] Broeren, A. P., Whalen, E. A., Busch, G. T., and Bragg, M. B., "Aerodynamic simulation of runback ice accretion," *Journal of Aircraft*, Vol. 47, No. 3, 2010, pp. 924–939.

[10] Gurbacki, H., and Bragg, M., "Unsteady aerodynamic measurements on an iced airfoil," *40th AIAA Aerospace Sciences Meeting & Exhibit*, 2002, p. 241.

[11] Chung, J., and Addy, H., Jr, "A numerical evaluation of icing effects on a natural laminar flow airfoil," *38th Aerospace Sciences Meeting and Exhibit*, 2000, p. 96.

[12] Pan, J., and Loth, E., "Reynolds-averaged Navier-Stokes simulations of airfoils and wings with ice shapes," *Journal of aircraft*, Vol. 41, No. 4, 2004, pp. 879–891.

[13] Cao, Y., Chen, K., and Sheridan, J., "Flowfield simulation and aerodynamic performance analysis of complex iced aerofoils with hybrid multi-block grid," *Proceedings of the Institution of Mechanical Engineers, Part G: Journal of Aerospace Engineering*, Vol. 222, No. 3, 2008, pp. 417–422.

[14] Pan, J., and Loth, E., "Detached eddy simulations for iced airfoils," *Journal of aircraft*, Vol. 42, No. 6, 2005, pp. 1452–1461.

[15] Mogili, P., Thompson, D., Choo, Y., and Addy, H., "RANS and DES Computations for a Wing with Ice Accretion," *43rd AIAA Aerospace Sciences Meeting and Exhibit*, 2005, p. 1372.

[16] Lorenzo, A., Valero, E., and De-Pablo, V., "DES/DDES post-stall study with iced airfoil," *49th AIAA aerospace sciences meeting including the new horizons forum and aerospace exposition*, 2011, p. 1103.

[17] Zhang, Y., Habashi, W. G., and Khurram, R. A., "Zonal detached-eddy simulation of turbulent unsteady flow over iced airfoils," *Journal of Aircraft*, Vol. 53, No. 1, 2016, pp. 168–181.

[18] Alam, M., Thompson, D. S., and Walters, D. K., "Hybrid Reynolds-Averaged Navier–Stokes/Large-Eddy simulation models for flow around an iced wing," *Journal of aircraft*, Vol. 52, No. 1, 2015, pp. 244–256.

[19] Xiao, M., Zhang, Y., and Zhou, F., "Numerical study of iced airfoils with horn features using large-eddy simulation," *Journal of Aircraft*, Vol. 56, No. 1, 2019, pp. 94–107.

[20] Xiao, M., Zhang, Y., and Zhou, F., "Numerical investigation of the unsteady flow past an Iced multi-element airfoil," *AIAA Journal*, Vol. 58, No. 9, 2020, pp. 3848–3862.

[21] Larsson, J., Kawai, S., Bodart, J., and Bermejo-Moreno, I., "Large eddy simulation with modeled wall-stress: recent progress and future directions," *Mechanical Engineering Reviews*, Vol. 3, No. 1, 2016, pp. 15–00418.

[22] Kiris, C. C., Housman, J. A., Barad, M. F., Brehm, C., Sozer, E., and Moini-Yekta, S., "Computational framework for launch, ascent, and vehicle aerodynamics (LAVA)," *Aerospace Science and Technology*, Vol. 55, 2016, pp. 189–219.

[23] Weiss, P.-É., and Deck, S., "On the coupling of a zonal body-fitted/immersed boundary method with ZDES: application to the interactions on a realistic space launcher afterbody flow," *Computers & Fluids*, Vol. 176, 2018, pp. 338–352.

[24] Busch, G., Broeren, A., and Bragg, M., "Aerodynamic Fidelity of Sub-scale Two-Dimensional Ice Accretion Simulations," *26th AIAA Applied Aerodynamics Conference*, 2008, p. 7062.

[25] Kiris, C. C., Ghate, A. S., Duensing, J. C., Browne, O. M., Housman, J. A., Stich, G.-D., Kenway, G., Fernandes, L. S., and Machado, L. M., "High-Lift Common Research Model: RANS, HRLES, and WMLES perspectives for CLmax prediction using LAVA," *AIAA SCITECH 2022 Forum*, 2022, p. 1554.

[26] Deck, S., and Renard, N., "Towards an enhanced protection of attached boundary layers in hybrid RANS/LES methods," *Journal of Computational Physics*, Vol. 400, 2020, p. 108970.

[27] Spalart, P. R., Deck, S., Shur, M. L., Squires, K. D., Strelets, M. K., and Travin, A., "A new version of detached-eddy simulation, resistant to ambiguous grid densities," *Theoretical and computational fluid dynamics*, Vol. 20, No. 3, 2006, pp. 181–195.

[28] Deck, S., "Recent improvements in the zonal detached eddy simulation (ZDES) formulation," *Theoretical and Computational Fluid Dynamics*, Vol. 26, No. 6, 2012, pp. 523–550.

[29] Spalart, P., and Allmaras, S., "A one-equation turbulence model for aerodynamic flows," *30th aerospace sciences meeting and exhibit*, 1992, p. 439.

[30] Kiris, C. C., Stich, D., Housman, J. A., Kocheemoolayil, J. G., Barad, M. F., and Cadieux, F., "Application of Lattice Boltzmann and Navier-Stokes methods to NASA's wall mounted hump," *2018 Fluid Dynamics Conference*, 2018, p. 3855.

[31] Housman, J. A., Stich, G.-D., Kocheemoolayil, J. G., and Kiris, C. C., "Predictions of slat noise from the 30P30N at high angles of attack using zonal hybrid RANS-LES," *25th AIAA/CEAS Aeroacoustics Conference*, 2019, p. 2438.

[32] Ghate, A. S., Kenway, G. K., Stich, G.-D., Browne, O. M., Housman, J. A., and Kiris, C. C., "Transonic lift and drag predictions using Wall-Modelled Large Eddy Simulations," *AIAA Scitech 2021 Forum*, 2021, p. 1439.

[33] Browne, O. M., Housman, J. A., Kenway, G. K., Ghate, A. S., and Kiris, C. C., "A Hybrid RANS-LES Perspective for the High Lift Common Research Model Using LAVA," *AIAA AVIATION 2022 Forum*, 2022, p. 3523.

[34] Piomelli, U., and Balaras, E., "Wall-layer models for large-eddy simulations," *Annual review of fluid mechanics*, Vol. 34, No. 1, 2002, pp. 349–374.

[35] Piomelli, U., "Wall-layer models for large-eddy simulations," *Progress in aerospace sciences*, Vol. 44, No. 6, 2008, pp. 437–446.

[36] Bose, S. T., and Park, G. I., "Wall-modeled large-eddy simulation for complex turbulent flows," *Annual review of fluid mechanics*, Vol. 50, 2018, pp. 535–561.

[37] Vreman, A., "An eddy-viscosity subgrid-scale model for turbulent shear flow: Algebraic theory and applications," *Physics of fluids*, Vol. 16, No. 10, 2004, pp. 3670–3681.

[38] Ghate, A. S., Housman, J. A., Stich, G.-D., Kenway, G., and Kiris, C. C., "Scale resolving simulations of the NASA Juncture Flow Model using the LAVA solver," *AIAA Aviation 2020 Forum*, 2020, p. 2735.

[39] Stich, G.-D., Housman, J. A., Ghate, A. S., and Kiris, C. C., "Jet Noise Prediction with Large-Eddy Simulation for Chevron Nozzle Flows," *AIAA Scitech 2021 Forum*, 2021, p. 1185.

[40] Stich, G.-D., Ghate, A. S., Housman, J. A., and Kiris, C. C., "Wall Modeled Large Eddy Simulations for NASA's jet noise consensus database of single-stream, round, convergent jets." *AIAA SCITECH 2022 Forum*, 2022, p. 0684.

[41] Stich, G.-D., Ghate, A. S., Housman, J. A., and Kiris, C. C., "Wall-Modeled Large-Eddy Simulations of Jet Noise in Flight Conditions," *28th AIAA/CEAS Aeroacoustics Conference*, 2022.

[42] Wong, M. L., K. Kenway, G., Ghate, A. S., Stich, G.-D., and Kiris, C. C., "Predictions of LAGOON Nose Landing Gear Flow and Noise using Wall-Modeled Large Eddy Simulations," *28th AIAA/CEAS Aeroacoustics 2022 Conference*, 2022, p. 2850.

[43] Wong, M. L., and Lele, S. K., "High-order localized dissipation weighted compact nonlinear scheme for shock-and interface-capturing in compressible flows," *Journal of Computational Physics*, Vol. 339, 2017, pp. 179–209.

[44] Shu, C.-W., and Osher, S., "Efficient implementation of essentially non-oscillatory shock-capturing schemes, II," *Journal of Computational Physics*, Vol. 83, No. 1, 1989, pp. 32–78.

[45] Mochel, L., Weiss, P.-É., and Deck, S., "Zonal immersed boundary conditions: application to a high-Reynolds-number afterbody flow," *AIAA journal*, Vol. 52, No. 12, 2014, pp. 2782–2794.

[46] Broeren, A. P., Woodard, B., Diebold, J. M., and Moens, F., "Low-Reynolds number aerodynamics of an 8.9% scale semispan swept wing for assessment of icing effects," *9th AIAA Atmospheric and Space Environments Conference*, 2017, p. 4372.

[47] Stebbins, S., Loth, E., Broeren, A., Potapczuk, M., and Porter, C., "Aerodynamics of a common research model wing with leading-edge ice shape," *Journal of Aircraft*, Vol. 58, No. 4, 2021, pp. 894–906.

[48] Marongiu, C., Vitagliano, P., Zanazzi, G., and Narducci, R., "Aerodynamic analysis of an iced airfoil at medium/high Reynolds number," *AIAA journal*, Vol. 46, No. 10, 2008, pp. 2469–2478.

[49] Broeren, A. P., Addy Jr, H. E., Bragg, M. B., Busch, G. T., and Montreuil, E., "Aerodynamic simulation of ice accretion on airfoils," Tech. rep., 2011.

[50] Lumley, J. L., "The structure of inhomogeneous turbulent flows," *Atmospheric turbulence and radio wave propagation*, 1967, pp. 166–178.

[51] Towne, A., Schmidt, O. T., and Colonius, T., "Spectral proper orthogonal decomposition and its relationship to dynamic mode decomposition and resolvent analysis," *Journal of Fluid Mechanics*, Vol. 847, 2018, pp. 821–867.

[52] Schmidt, O. T., and Colonius, T., "Guide to spectral proper orthogonal decomposition," *Aiaa journal*, Vol. 58, No. 3, 2020, pp. 1023–1033.

[53] Lumley, J. L., "Stochastic tools in turbulence," 1970.

[54] Nekkanti, A., and Schmidt, O. T., "Frequency–time analysis, low-rank reconstruction and denoising of turbulent flows using SPOD," *Journal of Fluid Mechanics*, Vol. 926, 2021.